Ultrastretchable, fatigue-resistant eutectogel with hierarchical bonding for advanced wearable monitoring

Min Jeong Kim[1,2] · Sung Ho Cho[1,2] · Soong Ju Oh[2] · Sang Woo Kim[1]

[1] Clean Energy Research Center, Korea Institute of Science and Technology (KIST), Seoul 02792, Republic of Korea

[2] Department of Materials Science and Engineering, Korea University, Seoul, 02841, Republic of Korea

AUTHOR INFORMATION

Corresponding Author

*E-mail: swkim@kist.re.kr. Phone: +82-2-958-5526. Fax: +82-2-958-5219

List of Supplementary Tables, Figures, and Movies

Supplementary **Figure S1**. Photographs of fabricated eutectogels (DMC 3) in various shapes and sizes: (a) square (125 × 125 mm) and (b) circular (φ58 mm). Optical microscope images of MC-type conductors (MC 1–4) with varying PEDOT:PSS contents: (c) 4.1 wt%, (d) 5.2 wt%, (e) 7.0 wt%, and (f) 8.0 wt%.

Supplementary **Figure S2.** Particle size distribution of DMC conductors (DMC 1–4) with increasing PEDOT:PSS contents: (a) 4.1 wt%, (b) 5.2 wt%, (c) 7.0 wt%, and (d) 8.0 wt%.

Supplementary **Figure S3.** (a) Optical transmittance of eutectogel conductors; (b) Swelling ratio of eutectogel conductors as a function of time (c) Electrical conductivity of DMC 3 as a function of swelling ratio measured by the four-point probe method; (d) Stress-strain curves of DMC 3 at various swelling ratios.

Supplementary **Figure S4**. XPS spectra of (a) IC, (b) MC 3, (c) DIC, and (d) DMC 3 sensors.

Supplementary **Figure S5**. XPS O *1s* spectra of (a) MC 1, (b) MC 2, (c) MC 3, and (d) MC 4 sensors.

Supplementary **Figure S6.** XPS O *1s* spectra of (a) IC, (b) DIC, (c) MC 3, and (d) DMC 3 sensors.

Supplementary **Figure S7.** Mechanical hysteresis of (a) IC, (b) MC 3, (c) DMC 3 sensors under different strains at 1 Hz. Mechanical hysteresis across various stretch-relaxation cycles for (d) IC, (e) MC 3, and (f) DMC 3 under 600% strain (λ_{max}=7). (g) Energy release rate of uncut sensors in the initial and steady state cycles at λ_{max}=7.

Supplementary **Figure S8.** Enhanced healing efficiency of DMC 3 under both physical compression and thermal annealing conditions.

Supplementary **Figure S9.** Response signals of the sensors during cyclic stretch–release motions at 50% strain under various strain rates: (a, d) IC, (b, e) MC 3, and (c, f) DMC 3 at 4.33Hz; (g) IC, (h) MC 3, and (i) DMC 3 at 1 Hz; (j) IC, (k) MC 3, and (l) DMC 3 at 0.17 Hz.

Supplementary **Figure S10**. Response signals of the sensors during cyclic stretch–release motions at 100% strain under different strain rates: (a, d) IC, (b, e) MC 3, and (c, f) DMC 3 at 4.33Hz; (g) IC, (h) MC 3, and (i) DMC 3 at 1 Hz; (j) IC, (k) MC 3, and (l) DMC 3 at 0.17 Hz.

Supplementary **Figure S11**. Stress–strain curves and response signals of the uncut MC 3 sensor after autonomous recovery following 100,000 cycles at 1 Hz under strains of (a, c) 50% and (b, d) 100% strain.

Supplementary **Figure S12**. Stress–strain curves and response signals of the uncut DMC 3 sensor after autonomous recovery following 100,000 stretch–release cycles at 1 Hz under strains of (a, c) 50%, (b, d) 100%, and (c, f) 150%.

Supplementary **Figure S13**. Relative resistance changes ($\Delta R/R_0$) of DMC 3 sensors measured at room temperature under varying relative humidity conditions: (a) 30% RH, (b) 50% RH, (c) 70% RH, and (d) 90% RH. The sensors were placed in a temperature-controlled chamber and stabilized at each humidity level for 5 minutes before applying repeated on-off cycles to obtain $\Delta R/R_0$ from the I-V curve. The measurements indicate minimal resistance variation across the tested humidity range, highlighting the humidity-resistant performance of DMC 3 sensors.

Supplementary **Figure S14**. Relative resistance changes ($\Delta R/R_0$) of DMC 3 sensors at room temperature under different swelling ratios: (a) original, (b) 10%, (c) 20%, (d) 30%, (e) 50%, and (f) $\Delta R/R_0$ versus stretching cycles at different swelling ratios.

Supplementary **Figure S15**. Schematic of fatigue cyclic test conditions for (a) uncut and (b) pre-cut sample with single notch. Rectangular samples (50×30×1.0 mm^3) were clamped in two rigid grips and mounted in a tensile testing machine with a 100 N load cell. The length (H = 10 mm) and width (W = 30 mm) of samples in the undeformed state were used for cyclic stretch tests. Fatigue-resistance tests were performed using the single-notch method with a 10 mm pre-cut crack length, subjected to cyclic stretching at maximum stretch (λ_{max}) at a crosshead speed of 750 mm/min.

Supplementary **Figure S16**. Crack growth (Δc) over fatigue cycles (N) at various λ_{max} levels for single-notch sensors: (a) IC, (b) DIC, (c) MC 3, and (d) DMC 3.

Supplementary **Figure S17**. Variation of crack extension rate ($\Delta c/\Delta N$) with stretch (λ_{max}) for single-notch sensors.

Supplementary **Figure S18**. Crack extension rate ($\Delta c/\Delta N$) as a function of energy release rate (G) and fatigue threshold (G_c) for the single-notch DIC sensor.

Supplementary **Figure S19**. Progression of pre-crack length in single-notch IC sensors during fatigue cycling tests at various λ_{max} levels.

Supplementary **Figure S20**. Progression of pre-crack length in single-notch DIC sensors during fatigue cycling tests at various λ_{max} levels.

Supplementary **Figure S21**. Progression of pre-crack length in single-notch MC 3 sensors during fatigue cycling tests at various λ_{max} levels.

Supplementary **Figure S22**. Progression of pre-crack length in single-notch DMC 3 sensors during fatigue cycling tests at various λ_{max} levels.

Supplementary **Figure S23**. Photographs showing self-healing of (a) single-notch DIC at λ_{max}=1.75 and (b) single-notch DMC 3 at λ_{max}=1.5 during cyclic stretching from 10 to 8,000 cycles.

Supplementary **Figure S24**. Response signals from the skin-attached DMC 3 sensors with different swelling ratios monitoring various human physiological movements. Ankle movements: (a) 10% and (c) 50%; Wrist movements: (b) 10% and (d) 50%.

Supplementary **Figure S25**. Relative resistance changes of the uncut DMC 3 sensor over 7,000 stretch-release cycles under 300% strain (λ_{max} = 4) at 1 Hz (top). The bottom graph shows the stable resistance response of the DMC 3 sensor during cyclic testing.

Supplementary **Movie 1**. Tensile stress–strain test of the DMC 3 sensor (16x speed).

Supplementary **Movie 2**. Skin adhesion test of the DMC 3 sensor.

Supplementary **Movie 3**. Stretching test of the DMC 3 sensor.

Supplementary **Movie 4**. Response signal monitoring by the IC sensor during cyclic fatigue test over 100,000 stretch-release cycles under 50% strain at 1 Hz.

Supplementary **Movie 5**. Response signal monitoring by the MC 3 sensor during cyclic fatigue test over 100,000 stretch-release cycles under 150% strain at 1 Hz.

Supplementary **Movie 6**. Response signal monitoring by the DMC 3 sensor during cyclic fatigue test over 100,000 stretch-release cycles under 200% strain at 1 Hz.

Supplementary **Movie 7**. Monitoring of current signals from the DMC 3 sensor attached to the wrist during repetitive bending and extension movements.

Supplementary **Movie 8**. Monitoring of current signals from the DMC 3 sensor during repetitive handwriting movements.

Table S1. The component details of ionic eutectogels and organic mixed ionic–electronic conductor (OMIEC) eutectogels

Sample	ChCl (wt%)	Gly (wt%)	AA (wt%)	Initiator (wt%)	PEG(575)DA (wt%)	PEDOT:PSS (wt%)
PEDOT:PSS film	0	0	0	0	0	100
IC	30.2	39.8	28.9	1.0	0.1	0
MC 1	28.4	37.5	28.9	1.0	0.1	4.1
MC 2	27.9	36.9	28.9	1.0	0.1	5.2
MC 3	27.2	35.8	28.9	1.0	0.1	7.0
MC 4	26.7	35.3	28.9	1.0	0.1	8.0
DIC	30.2	39.8	28.9	1.0	0.1	0
DMC 1	28.4	37.5	28.9	1.0	0.1	4.1
DMC 2	27.9	36.9	28.9	1.0	0.1	5.2
DMC 3	27.2	35.8	28.9	1.0	0.1	7.0
DMC 4	26.7	35.3	28.9	1.0	0.1	8.0

Abbreviations: ChCl: Choline chloride, Gly: Glycerol, AA: Acrylic acid, PEDOT:PSS: Poly(3,4-ethylenedioxythiophene):poly(styrene sulfonate), Photoinitiator: 2-oxoglutaric acid, Cross-linker: Poly(ethylene glycol) diacrylate (PEG(575)DA).

Table S2. FT-IR peak assignments of PEDOT:PSS film, IC, MC 3, and DMC 3 eutectogels

Functional groups	PEDOT:PSS (cm^{-1})	IC (cm^{-1})	DIC (cm^{-1})	MC 3 (cm^{-1})	DMC 3 (cm^{-1})
O─H stretching	3,408, 3,206	3,332, 3,339	3,331, 3,345 3,353	3,331, 3,345 3,353	3,332, 3,345, 3,370
CH_2 asymmetric, symmetric stretching (Gly, EG)	─	2,931 2,876	2,938 2876	2,931 2,876	2,934 2,876
C═O stretching (PAA)	─	1,723	1,719	1,720	1,717
C═C asymmetric stretching	1,598 (PSS), 1,520 (PEDOT)	─	─	─	─
N^+─$(CH_3)_3$ bending(ChCl)	─	1,477	1,476	1,477	1,473
CH_2 bending (PAA, Gly, EG)	─	1,453	1,452	1,452	1,455
C─C inter-ring stretching (PEDOT)	1,270	─	─	─	─
C─O─H bending (EG, Gly, PAA)	─	1,415	1,412	1,415	1,412
C─O─H stretching (PAA, ChCl, Gly)	─	1,237	1,247	1,236	1,242
C─O stretching (ChCl)	─	1,171	1,176	1,170	1,175
S─O, S─phenyl (PSS)	1,162, 1,122	─	─	─	─
C─C─O (EG), C─O stretching (ChCl)	─	1,086	1,083	1,086	1,084
C─O─C (PEDOT)	1,057	─	─	─	─
O─S─O symmetric stretching (PSS)	1,010	─	─	─	─
C─C─O asymmetric stretching (Gly, EG)	─	1,042	1,037	1,042	1,039
N^+─C (ChCl)	─	956	954	956	956
C─S─C (PEDOT)	945, 859, 707	─	─	─	─
C─OH stretching (Gly)	─	923	922	923	923
CH_2 rocking vibration (EG)	─	─	881	─	882
C─C stretching (Gly/EG)	─	864	864	864	864

Table S3. FT-IR data for the OH stretching region (3,000–3,700 cm^{-1}), including (a) peak position (cm^{-1}) and (b) area ratio (%)

(a)

Functional groups	PEDOT:PSS (cm^{-1})	IC (cm^{-1})	DIC (cm^{-1})	MC 3 (cm^{-1})	DMC 3 (cm^{-1})
Free OH, Water	–	3,506	3,506	3,512	3,511
OH—SO_x^-(PSS)/ $PEDOT^+$	3,408	–	–	3,420	3,421
OH—OH	–	3,375	3,356	3,358	3,343
OH—Cl^-	–	3,250	3,216	3,259	3,260
OH—SO_x^- (PEDOT:PSS)	3,206	–	–	3,209	3,194
OH—COOH (PAA)	–	3,158	3,100	3,142	3,126
OH—SO_x^- (PEDOT:PSS)	3,039	–	–	3,040	3.044

(b)

Functional groups	PEDOT:PSS (%)	IC (%)	DIC (%)	MC 3 (%)	DMC 3 (%)
Free OH, Water	0	8.4	9.8	7.0	7.6
OH—SO_x^- (PEDOT:PSS)	55.4	0	0	13.5	16.3
OH—OH	0	60.4	62.5	48.6	51.0
OH—Cl^-	0	27.9	25.6	19.9	14.5
OH—SO_x^- (PEDOT:PSS)	36.5	0	0	6.7	6.1
OH—COOH (PAA)	0	3.3	2.1	4.0	4.2
OH—SO_x^- (PEDOT:PSS)	8.0	0	0	0.3	0.1

Table S4. XPS peak assignments of the IC, DIC, MC 3, and DMC 3 eutectogels

Sample	State	Binding energy (eV)	Bonding		Proportion (%)
IC	O 1s	532.5	C—O		75.16
		533.1	C—OH		24.84
DIC	O 1s	532.4	C—O		65.13
		532.7	C—OH		34.87
MC 3	O 1s	531.5	O═S (PSS)		31.5
		532.2	C—O/C—O—C		48.43
		533.6	C—OH		20.07
	S 2p	163.1	C—S (PEDOT)	$2p_{3/2}$	42
		165.2		$2p_{1/2}$	
		167.8	S—O_x (PSS)	$2p_{3/2}$	58
		168.9		$2p_{1/2}$	
DMC 3	O 1s	531.5	O═S (PSS)		18.9
		532.23	C—O/C—O—C		56.26
		533.4	C—OH		24.84
	S 2p	163.2	C—S (PEDOT)	$2p_{3/2}$	61
		165.1		$2p_{1/2}$	
		168.1	S—O_x (PSS)	$2p_{3/2}$	39
		168.9		$2p_{1/2}$	

Table S5. Raman peak positions and assignments of MC 3 and DMC 3 eutectogels

Moiety	**MC 3 (cm^{-1})**	**DMC 3 (cm^{-1})**
$C_{\alpha}-C_{\alpha}$	1,263.1	1,260.8
$C_{\beta}-C_{\beta}$	1,368.8	1,367.7
$C_{\alpha}=C_{\beta}$	1,448.4	1,442.8
$C_{\alpha}=C_{\beta}$	1,501.6	1,503.8

Table S6. Quantitative Raman spectroscopy analysis of MC 3 and DMC 3 eutectogels

Sample	State	Shift (cm^{-1})	Bonding	Proportion (%)
MC 3	Quinoid	1,425.2	$C_\alpha - C_\beta$ symmetric	38.86
	Benzoid	1,447.8	$C_\alpha = C_\beta$ symmetric	61.14
DMC 3	Quinoid	1,428.5	$C_\alpha - C_\beta$ symmetric	51.61
	Benzoid	1,445.7	$C_\alpha = C_\beta$ symmetric	48.39

Table S7. Electrical and mechanical properties of ionic eutectogels and OMIEC eutectogels

Sample	PEDOT:PSS concentration (wt.%)	Conductivity (S/m)	Tensile strength (kPa)	Elongation at break (%)	Elastic modulus (kPa)
PEDOT:PSS film	100	13.1	–	–	–
IC	0	0.017	90±2.9	1,038±15.3	11±1.3
MC 1	4.1	0.032	90±4.4	1,134±14.8	14±0.8
MC 2	5.2	0.061	93±3.6	1,134±17.5	15 ±0.5
MC 3	7.0	0.19	95±4.3	1,600±21.3	17±1.1
MC 4	8.0	0.026	43±2.2	1,235±20.6	12±0.8
DIC	0	0.11	95±3.1	1,217±21.3	19±0.6
DMC 1	4.1	0.17	93±3.3	1,783±19.1	20±0.9
DMC 2	5.2	0.21	102±2.8	1,786±22.3	21±1.4
DMC 3	7.0	1.12	142±3.1	3,065±53.0	26±0.7
DMC 4	8.0	0.21	59±2.6	2,145±28.5	14±1.2

Table S8. Degree of electromechanical hysteresis (EMH) for eutectogel sensors under various strains at 1 Hz

Strain (%)	**IC**	**MC 3**	**DMC 3**
100	7.46±0.92	1.48±0.23	0.28 ±0.13
400	15.74±1.82	1.56±0.31	0.45 ±0.12
600	17.03±3.24	1. 65 ±0.06	0.57±0.04
700	17.37±1.87	1.91±0.6	0.9 ±0.27
1000	–	2.08±0.63	0.99 ±0.29
1300		2.11±0.89	1.01 ±0.52
1500		5.55±0.91	1.02±0.47
1600		–	3. 8 ±0.34
2000		–	7.97±0.56

Table S9. EMH across various stretch–release cycles for IC, MC 3, and DMC 3 sensors under various strains at 1 Hz

Strain (%)	Cycle	IC	MC 3	DMC 3
400	1	15.74±1.82		
	5	21.14±1.93		
	10	20.92±1.36		
	50	19.69±1.58		
	100	28.16±2.78		
600	1	17.03±3.24	1.65 ±0.06	0.57±0.04
	5	30±4.71	2.37 ±0.11	0.66±0.06
	10	–	2.42±0.17	0.77±0.05
	50		2.47±0.21	0.88±0.08
	100		2.77±0.28	1.75±0.10
1,000	1		1.56±0.31	0.8±0.33
	5		2.6±0.76	1.99±0.45
	10		3.35±0.83	3.13±0.57
	50		5.36±1.07	3.84±0.55
	100		5.64±1.02	4.37±0.81
1,500	1		5.55±0.91	1.02±0.47
	5		7.38±0.83	1.04±0.53
	10		11.51±1.02	3.35±0.58
	50		11.61±1.38	3.44±0.62
	100		12.09±1.11	3.47±0.84
2,000	1			7.97±1.31
	5			10.51±1.85
	10			14.94±1.94
	50			17.61±2.13
	100			–

Table S10. Comparison of EMH between the present study and previously reported strain sensors

Material	Strain (%)	Resistance hysteresis (%)	Supplementary reference
IC	100	7.5	This work
	400	7.9	
	700	17.4	
MC 3	100	1.5	This work
	400	1.6	
	700	1.9	
	1,000	2.1	
	1,300	2.1	
DMC 3	100	0.3	This work
	400	0.5	
	700	0.9	
	1,000	1.0	
	1,300	1.0	
	1,500	1.0	
	1,600	3.8	
	2,000	8.0	
ChCl/AA/PEDOT:PSS eutectogel	100	23.1	[1]
	300	19.1	
	500	42.6	
	800	55.9	
H- ChCl/AA/PEDOT:PSS eutectogel	100	12.5	[1]
	300	11.6	
	500	30.3	
	800	45.9	
PEDOT:PSS/PVA hydrogel	300	1.5	[2]
CNT/PEDOT:PSS@NR microfiber	100	10.8	[3]
PEDOT:PSS–PAAm organogel	50	10.0	[4]

MWCNT/PEDOT:PSS based fiber	50	15.2	[5]
PEDOT:PSS on PDMS microchannel	30	9.2	[6]
VSNPs/PAAm/alginate hydrogel nanocomposites	100	2.4	[7]
K-carrageenan/PAAm hydrogel	1,000	9.6	[8]
PVA/AgNWs Bilayer hydrogel nanocomposites	250	7.0	[9]
MWCNT/silicone rubber conducting nanocomposites	50	3.0	[10]
	100	5.0	
	200	8.0	
	300	11	
POCL elastomer	300	1.0	[11]
EG–NaCl–Ecoflex ionogel	250	0.2	[12]

Table S11. Gauge factor (GF) of eutectogel sensors

Strain interval (%)	IC	MC 3	DMC 3
0–600	0.71	1.17	1.66
600–1000	1.47	1.97	2.45
1000–1400	–	2.67	–
1000–1600	–	–	3.91
1600–2000	–	–	1.8

Table S12. Response time of the IC sensor at various strain rates under 150% strain

Strain rate (Hz)	Response time (ms)	**Strain rate (Hz)**	Response time (ms)	**Strain rate (Hz)**	Response time (ms)
0.17	2,360	**1.83**	278	**3.5**	122
0.33	1,300	**2**	216	**3.67**	122
0.5	895	**2.17**	216	**3.83**	113
0.67	625	**2.33**	216	**4**	113
0.83	486	**2.5**	216	**4.17**	103
1	486	**2.67**	180	**4.33**	94
1.17	416	**2.83**	180		
1.33	347	**3**	150		
1.5	278	**3.17**	141		
1.67	278	**3.33**	132		

Table S13. Response time of the MC 3 sensor at various strain rates under 150% strain

Strain rate (Hz)	Response time (ms)	**Strain rate (Hz)**	Response time (ms)	**Strain rate (Hz)**	Response time (ms)
0.17	1,805	**1.83**	216	**3.5**	113
0.33	1,180	**2**	216	**3.67**	103
0.5	833	**2.17**	180	**3.83**	103
0.67	625	**2.33**	180	**4**	95
0.83	486	**2.5**	180	**4.17**	95
1	416	**2.67**	144	**4.33**	94
1.17	347	**2.83**	144		
1.33	347	**3**	144		
1.5	278	**3.17**	144		
1.67	278	**3.33**	113		

Table S14. Response time of the DMC 3 sensor at various strain rates under 150% strain

Strain rate (Hz)	Response time (ms)	**Strain rate (Hz)**	Response time (ms)	**Strain rate (Hz)**	Response time (ms)
0.17	1,805	**1.83**	208	**3.5**	103
0.33	1,110	**2**	180	**3.67**	103
0.5	763	**2.17**	180	**3.83**	94
0.67	555	**2.33**	180	**4**	94
0.83	486	**2.5**	144	**4.17**	84
1	416	**2.67**	144	**4.33**	84
1.17	347	**2.83**	144		
1.33	277	**3**	144		
1.5	277	**3.17**	131		
1.67	208	**3.33**	113		

Table S15. Relative resistance change, response time, and mechanical properties of the uncut IC sensor during self-healing following 100,000 fatigue cycles under 50% strain at 1 Hz

Self-healing time (h)	**Stretch─release cycle**	**0 (pristine)**	**100,000**
	Applied strain	0%	50%
0	$\Delta R/R_0$	0	0.337
	Response time (ms)	486	486
	Elongation (%)	1,038 (±15.3)	612
	Tensile strength (kPa)	90 (±2.9)	36
12	$\Delta R/R_0$	−	0.18
	Response time (ms)	−	486
	Elongation (%)	−	1,017
	Tensile strength (kPa)	−	44

Table S16. Relative resistance change, response time, and mechanical properties of the uncut MC 3 sensor during self-healing following 100,000 fatigue cycles under various strains at 1 Hz

Self-healing time (h)	**Stretch–release cycle**	**0 (Pristine)**	**100,000**		
	Applied strain	0%	50%	100%	150%
0	$\Delta R/R_0$	0	0.051	0.125	0.158
	Response time (ms)	416	416	416	486
	Elongation (%)	1,600 (±21.3)	1,590	1,586	1,262
	Tensile strength (kPa)	95 (±4.3)	80	67	89
12	$\Delta R/R_0$	–	0.009	0.011	0.012
	Response time (ms)	–	416	416	416
	Elongation (%)	–	1,608	1,615	1,614
	Tensile strength (kPa)	–	98	94	92

Table S17. Relative resistance change, response time, and mechanical properties of the uncut DMC 3 sensor during self-healing following 100,000 fatigue cycles under various strains at 1 Hz

Self-heaing time (h)	Stretch─release cycle	0 (Pristine)	100,000			
	Applied strain	0%	50%	100%	150%	200%
0	$\Delta R/R_0$	0	0.048	0.098	0.156	0.646
	Response time (ms)	416	416	416	416	416
	Elongation (%)	3,065 (±53)	3,022	3,011	3,008	2,634
	Tensile strength (kPa)	142 (±3.1)	116	115	101	93
6	$\Delta R/R_0$	─	0.028	0.048	0.096	0.164
	Response time (ms)	─	416	416	416	416
	Elongation (%)	─	3,035	3,045	3,037	3,013
	Tensile strength (kPa)	─	135	126	122	125
12	$\Delta R/R_0$	─	0.009	0.011	0.012	0.032
	Response time (ms)	─	416	416	416	416
	Elongation (%)	─	3,064	3,059	3,042	3,119
	Tensile strength (kPa)	─	147	146	148	141

Table S18. Crack length (mm) of precut sensors during cyclic stretching

(mm)

Sample	IC				DIC			
Stretch (λ) / Cycle	**1.25**	**1.5**	**1.75**	**2**	**1.25**	**1.5**	**1.75**	**2**
0	10	10	10	10	10	10	10	10
1,000	10	10.5	10.5	12	10	10.1	10.1	10.7
2,000	10	10.5	11	13	10	10.2	10.4	11.2
3,000	10	10.5	11.5	14	10	10.2	10.8	11.6
4,000	10	10.5	12.2	15	10	10.3	11.1	11.9
5,000	10	10.5	12.3	16	10	10.3	11.4	12.4
6,000	10	11	12.6	17	10	10.3	11.6	12.6
7,000	10	11	12.8	18	10	10.4	11.7	12.6
8,000	10	11	-	-	10	10.4	11.9	12.6
9,000	10	11	-	-	10	-	-	-
10,000	10	11	-	-	10	-	-	-

Sample	MC 3				DMC 3			
Stretch (λ) / Cycle	**1.25**	**1.5**	**1.75**	**2**	**1.25**	**1.5**	**1.75**	**2**
0	10	10	10	10	10	10	10	10
1,000	10	10	11	14.5	10	10.1	10.7	10.8
2,000	10	10	11	17	10	10.2	11.2	11.3
3,000	10	10	11.5	19	10	10.3	11.7	12.2
4,000	10	10	12	20	10	10.4	11.8	13.1
5,000	10	10.5	13	22	10	10.4	12.1	13.2
6,000	10	10.5	13.5	24	10	10.5	12.2	13.2
7,000	10	10.5	13.5	27	10	10.5	12.5	13.3
8,000	10	10.5	13.5	30	10	10.5	12.5	13.3
9,000	10	10.5	13.5	-	10	-	-	-
10,000	10	10.5	13.5	-	10	-	-	-

Table S19. Crack extension rate (Δc/ΔN) for uncut and precut sensors under cyclic stretching

Stretch (λ)		Crack Extension rate Δc/ΔN (μm/cycle)			
		IC	**DIC**	**MC3**	**DMC3**
Non-notch	**1.5**	0	0	0	0
Single notch	**1.25**	0	0	0	0
	1.5	0.167	0.055	0.033	0.085
	1.75	0.464	0.252	0.561	0.443
	2	1.5	0.440	2.833	0.673

Table S20. Energy release rate (G) for uncut and precut sensors under cyclic stretching

Stretch (λ)		**Energy release rate, G (J/m^2)**			
		IC	**DIC**	**MC3**	**DMC3**
Non-notch	**1.5**	35.10	33.51	56.55	57.50
Notch	**1.25**	16.77	18.02	26.52	35.64
	1.5	38.45	45.66	64.49	84.69
	1.75	68.16	85.85	113.24	115.34
	2	106.78	93.99	189.87	127.63

Table S21. Summary of electrical and mechanical properties of eutectogel sensors

		IC	MC 3	DMC 3
Tensile strength (kPa)		90	95	142
Elongation (%)		1,038	1,600	3,065
Elastic Modulus (kPa)		11	17	26
Sensitivity [= GF] (%)		1.47	1.97	3.91
Electromechanical hysteresis at 100% strain (%)		7.5	1.5	0.3
Toughness (J/m^2)		4,429	8,808	20,337
Fatigue threshold, G_c (J/m^2)		26.6	56.7	83.4
Work of fracture (kJ/m^3)	No fatigue	495	1,005	3,085
	0 h*	150	775	1,547
	6 h**	-	-	2,385
	12 h***	295	1,043	3,060

*: Tensile tests were performed on IC, MC 3, and DMC 3 samples immediately after 100,000 cycles of fatigue testing at strains of 50%, 150%, and 200%, respectively.

**: Tensile tests were performed on IC, MC 3, and DMC 3 samples after 6 hours of self-healing following 100,000 cycles of fatigue testing at strains of 50%, 150%, and 200%, respectively.

***: Tensile tests were performed on IC, MC 3, and DMC 3 samples after 12 hours of self-healing following 100,000 cycles of fatigue testing at strains of 50%, 150%, and 200%, respectively.

Table S22. Comparison of fatigue life cycles between the present study and previously reported stretchable sensors under cyclic stretching in the uncut condition

Material	Elongation at break (%)	Max. GF	Response time (ms)	Fatigue life cycle (strain)	Suppl. Ref.
DMC 3	3,050	3.91	84(4.33Hz) 416(1 Hz)	>100,000 (200%) 46,177 (250%) 30,217 (300%)	This work
MC 3	1,600	2.67	94(4.33Hz) 416(1 Hz)	>100,000 (150%) 44,797 (200%) 12,098 (250%) 7,417 (300%)	This work
IC	1,038	1.47	94(4.33Hz) 486(1 Hz)	>100,000 (50%) 8,409 (100%) 5,929 (150%)	This work
ChCl/AA/PEDOT:PSS eutectogel	802	4.48	61	11,300 (50%) 4,799 (100%) 2,399 (150%)	[1]
H-ChCl/AA/PEDOT:PSS eutectogel	964	3.15	40	100,000 (50%) 60,000 (100%) 5,949 (150%)	[1]
PAAM/SA/MXene/PEDOT:PSS nanocomposite hydrogel	1,350	1.99	624	600 (50%)	[13]

PAM/HPMC/PEDOT:PSS polymer hydrogel	1,640	17.58	150	300 (100%)	[14]
PAM/CCMF/PEDOT:PSS composite hydrogel	837	0.31	400	1,100 (300%)	[15]
PAA–Al^{3+}/PEDOT:PSS/ZB polymer hydrogel	1,457	1.32	-	150 (100%)	[16]
Gr/PEDOT:PSS/MnO_2 NWs nanocomposites	320	1.2	79	5,000 (100%)	[17]
PDMS/CNT nanocomposites	100	3.1	-	5,000 (100%)	[18]
AgNPs/CNTs/PDA–TPU mat	640	2×10^6	-	1,000 (200%)	[19]
SA/LM/Amm ionic hydrogel	1,348	0.6	200	350 (200%)	[20]
PEDOT:PSS@CB/CNT–TPU membrane	910	5.6	2,300	4,000 (25%)	[21]
PVA/MWCNT/PEDOT:PSS nanocomposites on PDMS	50	5.2	20	10,000 (10%)	[22]
CNTs/PDA/Elastic Bands	920	129.2	220	10,000 (100%)	[23]
$Ti_3C_2T_x$ on PDMS	53	178.4	130	5,000 (20%)	[24]
PVA/PEDOT:PSS elastomer	30	110	40	400 (20%)	[25]
$Ti_3C_2T_x$–graphene on PDMS	74.1	190.8	130	10,000 (40%)	[26]
Graphene nanoplatelets–AgNWs on PDMS	22	41.5	50	1,000 (10%)	[27]
rGO–TPU fiber mat	200	79	200	6,000 (50%)	[28]
CBs/CNTs nanocomposites	50	2.18	125	1,000 (15%)	[29]
GWF (Graphene woven fabric)	3	223	72	1,000 (3%)	[30]

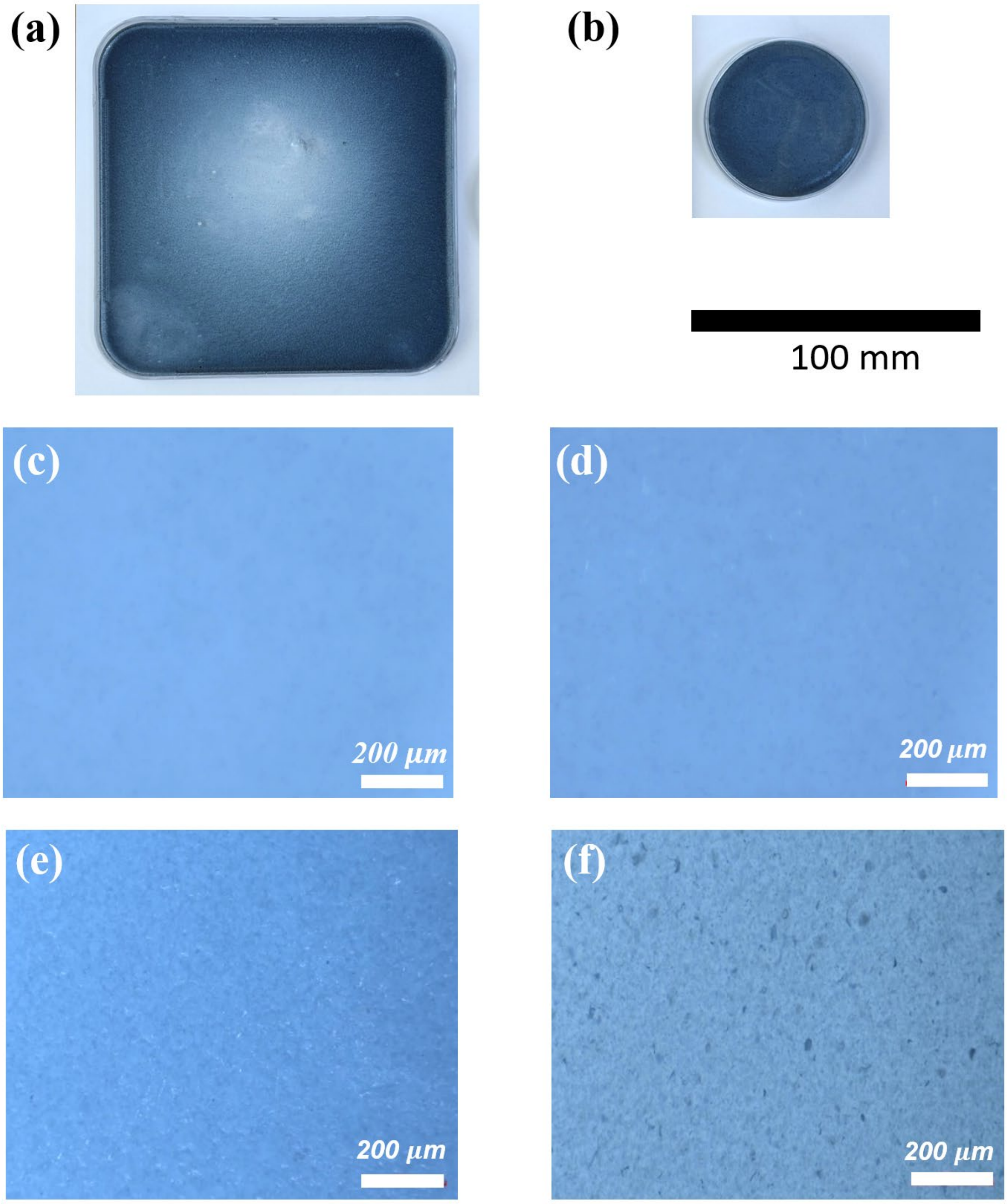

Figure S1. Photographs of fabricated eutectogels (DMC 3) in various shapes and sizes: (a) square (125 × 125 mm) and (b) circular (φ58 mm). Optical microscope images of MC-type conductors (MC 1–4) with varying PEDOT:PSS contents: (c) 4.1 wt%, (d) 5.2 wt%, (e) 7.0 wt%, and (f) 8.0 wt%.

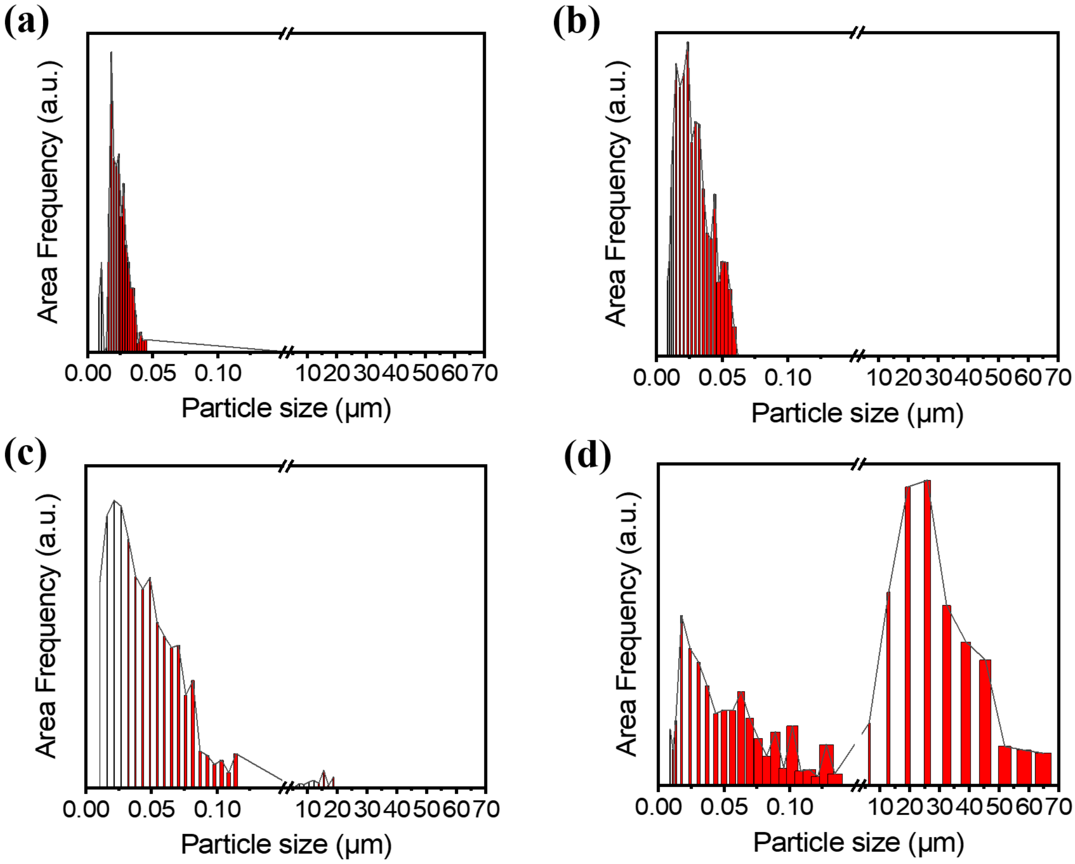

Figure S2. Particle size distribution of DMC conductors (DMC 1–4) with increasing PEDOT:PSS contents: (a) 4.1 wt%, (b) 5.2 wt%, (c) 7.0 wt%, and (d) 8.0 wt%..

Panels (a) and (b) show monomodal distributions with area-weighted average particle sizes of approximately 17 nm, indicating well-dispersed PEDOT:PSS domains in DMC 1 and DMC 2. Panel (c), corresponding to DMC 3 (7.0 wt%), exhibits a bimodal distribution consisting of a dominant nanoparticle population (mean diameter: 20.8 nm) and a minor fraction of micron-sized aggregates (~8.8 μm), marking the onset of aggregation. In panel (d), representing DMC 4 (8.0 wt%), the morphology is dominated by large PEDOT:PSS aggregates with an average size of 16.2 μm and a subpopulation of 17 nm particles, with an approximate 2:1 area frequency ratio (aggregates:nanoparticles). These results support the interpretation of a percolation threshold at 7.0 wt% and aggregation-induced network collapse beyond 8.0 wt%, as discussed in the main text and Fig. 3a.

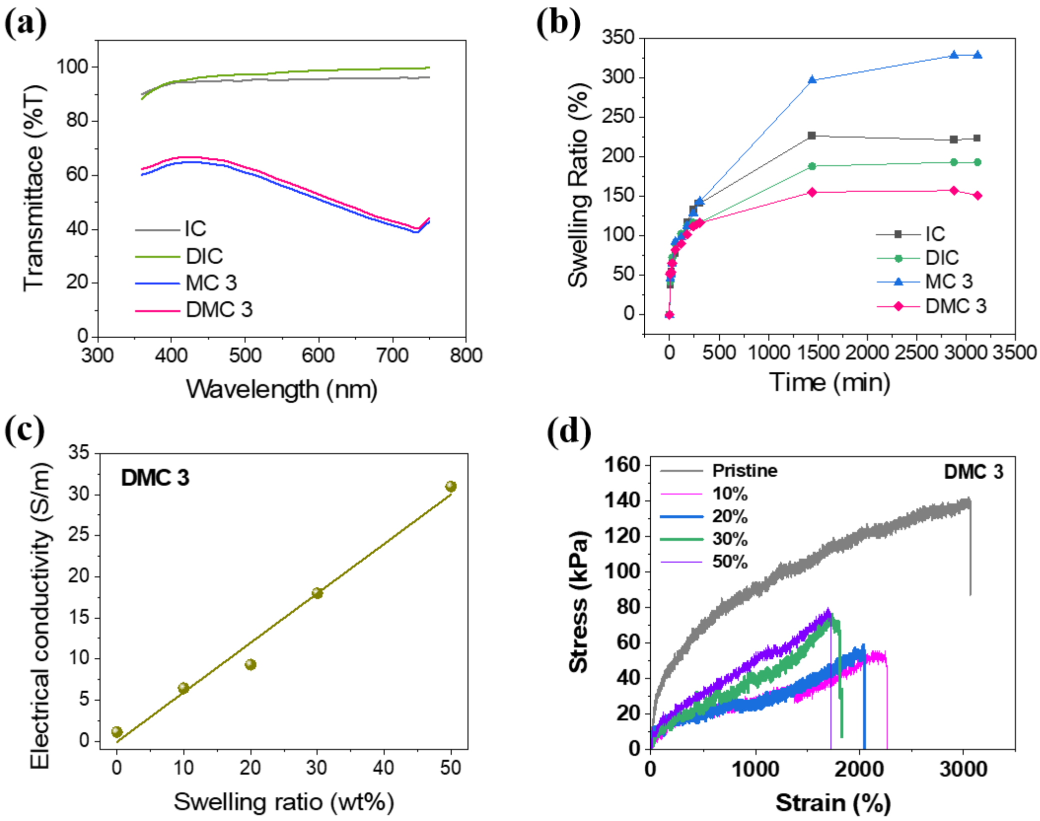

Figure S3. (a) Optical transmittance of eutectogel conductors; (b) Swelling ratio of eutectogel conductors as a function of time (c) Electrical conductivity of DMC 3 as a function of swelling ratio measured by the four-point probe method; (d) Stress-strain curves of DMC 3 at various swelling ratios.

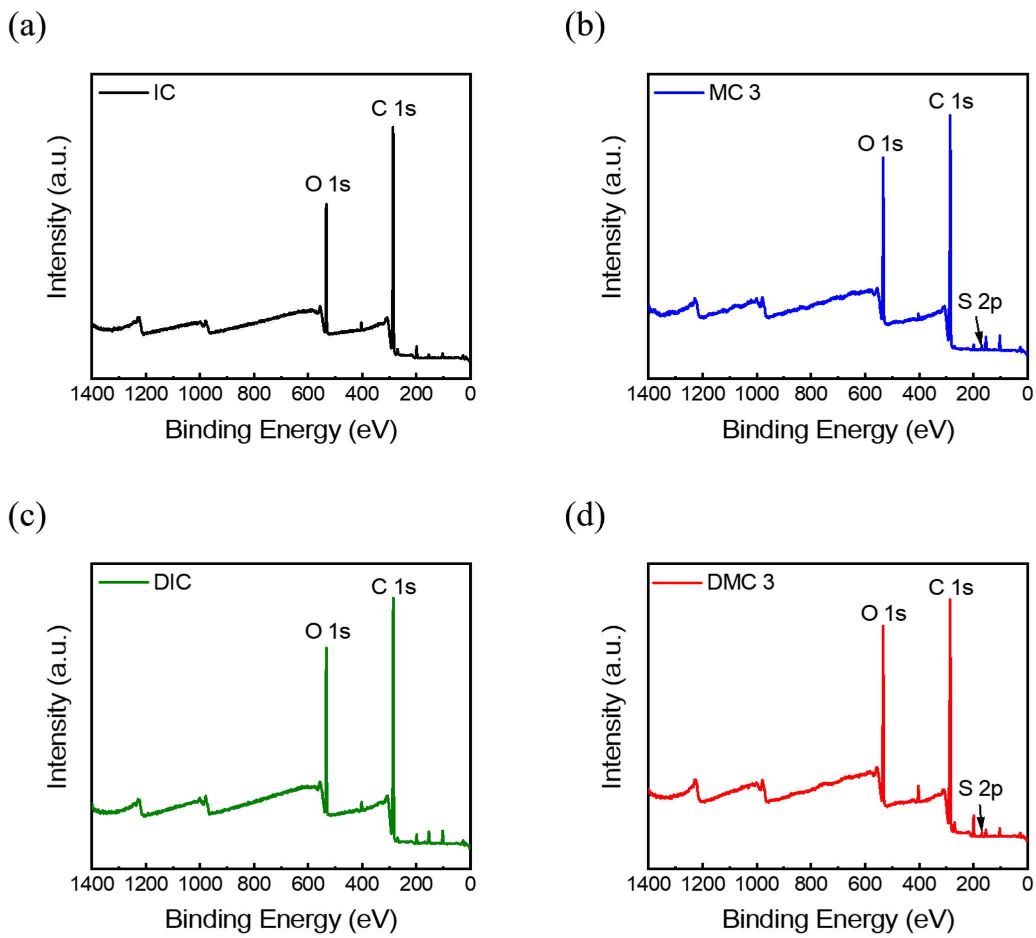

Figure S4. XPS spectra of (a) IC, (b) MC 3, (c) DIC, and (d) DMC 3 sensors.

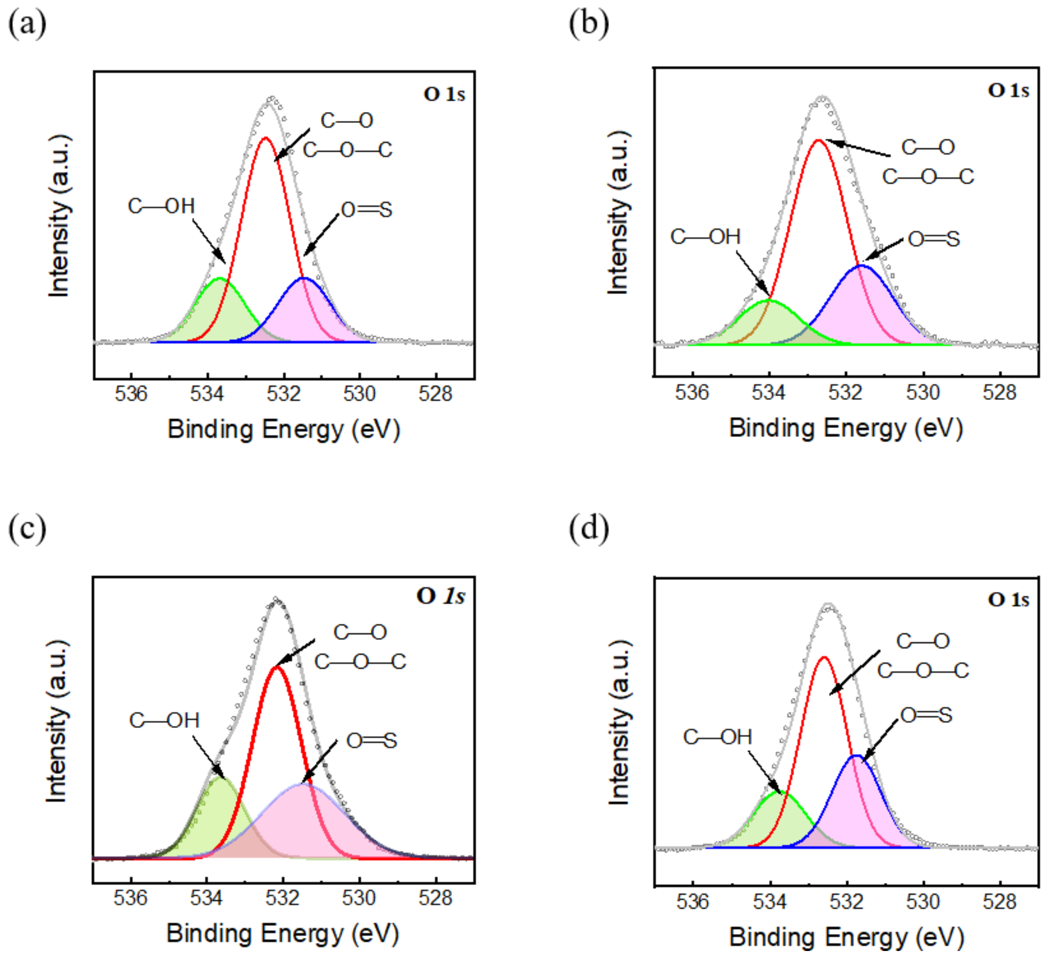

Figure S5. XPS O *1s* spectra of (a) MC 1, (b) MC 2, (c) MC 3, and (d) MC 4 sensors.

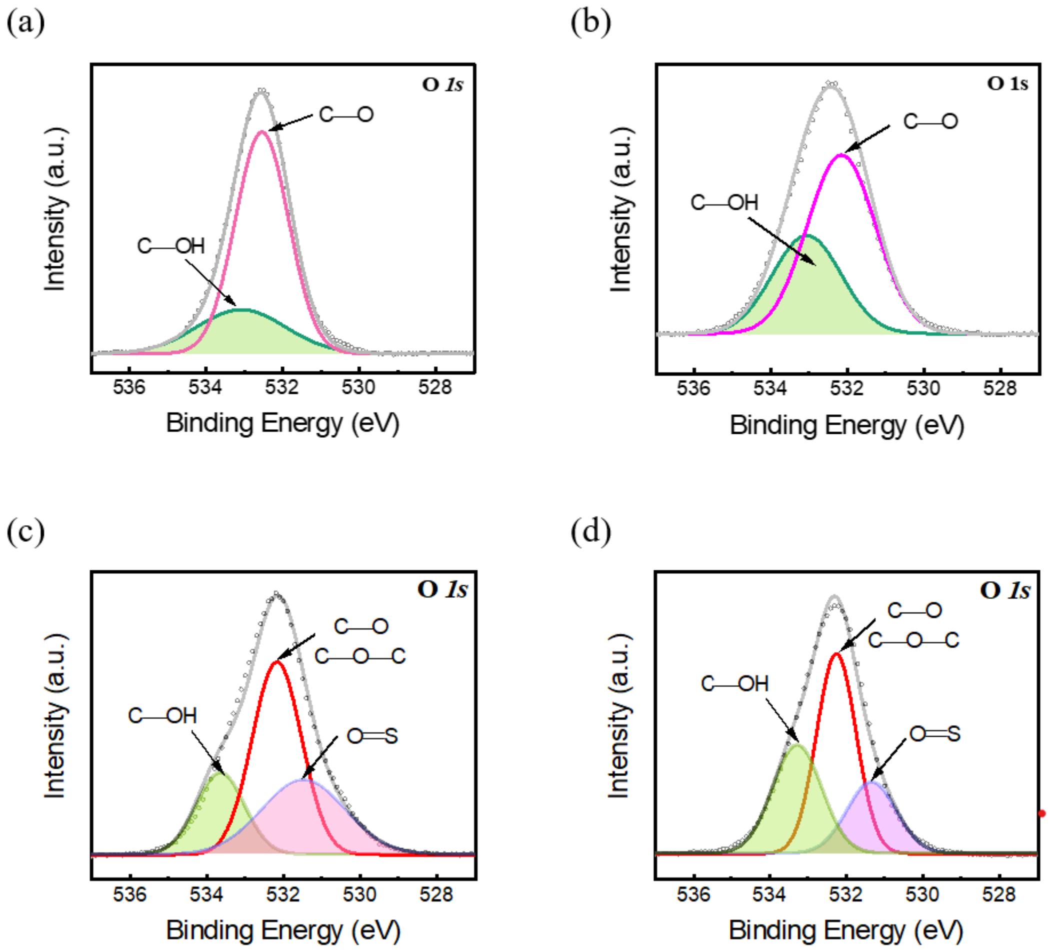

Figure S6. XPS O *1s* spectra of (a) IC, (b) DIC, (c) MC 3, and (d) DMC 3 sensors.

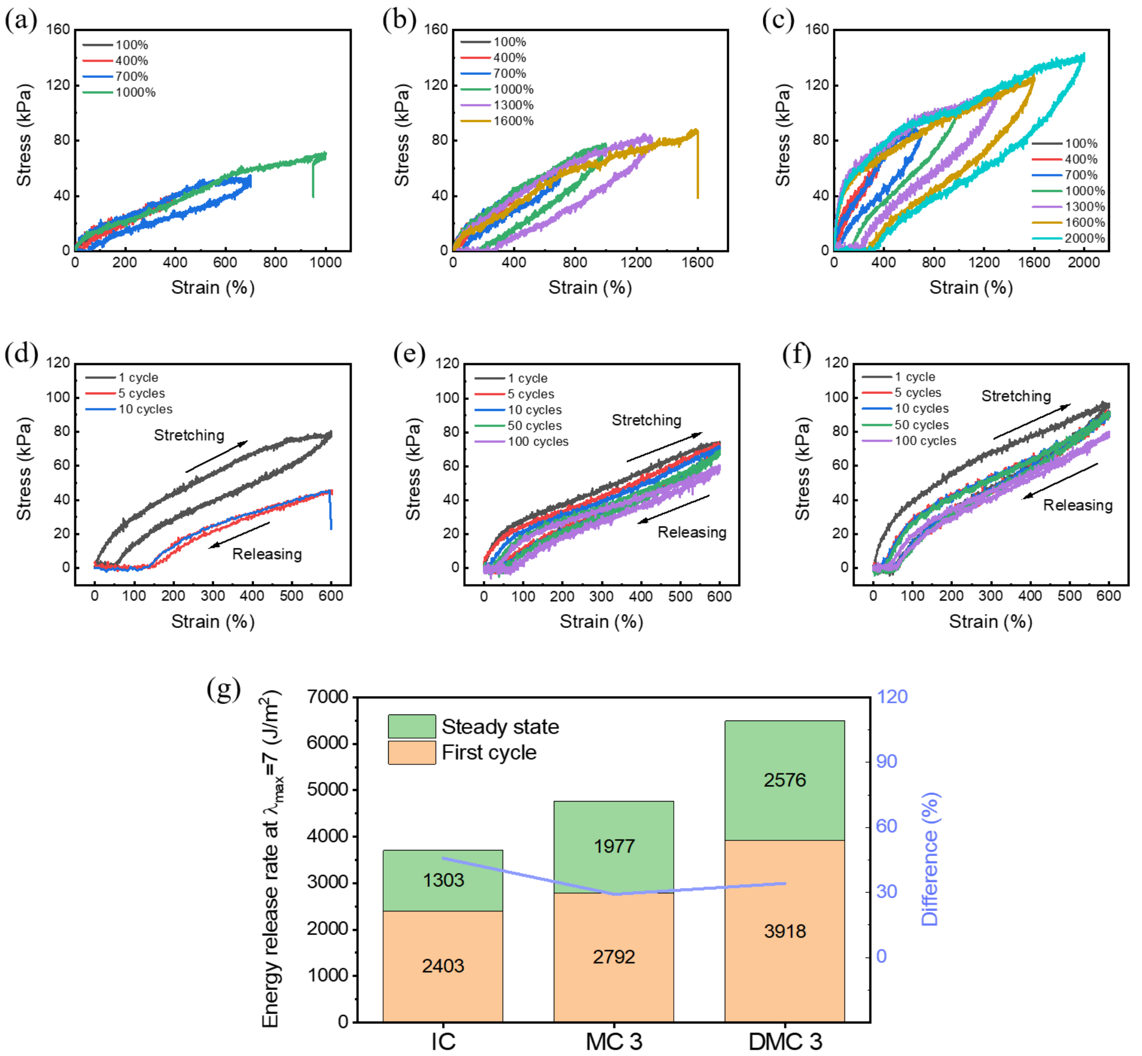

Figure S7. Mechanical hysteresis of (a) IC, (b) MC 3, (c) DMC 3 sensors under different strains at 1 Hz. Mechanical hysteresis across various stretch-relaxation cycles for (d) IC, (e) MC 3, and (f) DMC 3 under 600% strain (λ_{max}=7). (g) Energy release rate of uncut sensors in the initial and steady state cycles at λ_{max}=7.

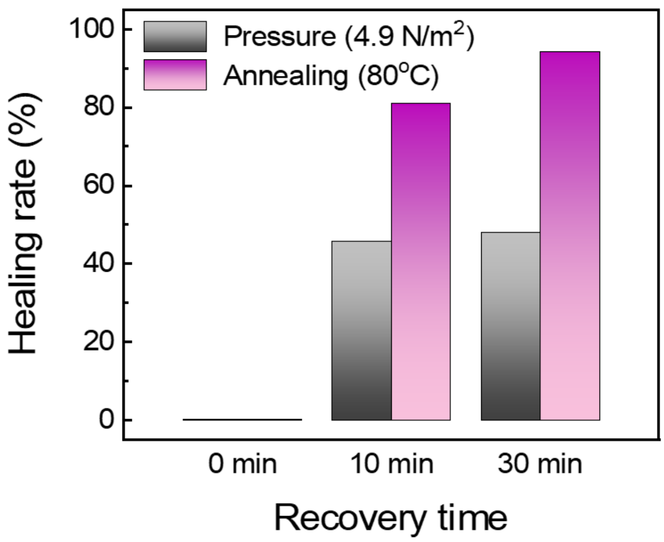

Figure S8. Enhanced healing efficiency of DMC 3 under both physical compression and thermal annealing conditions.

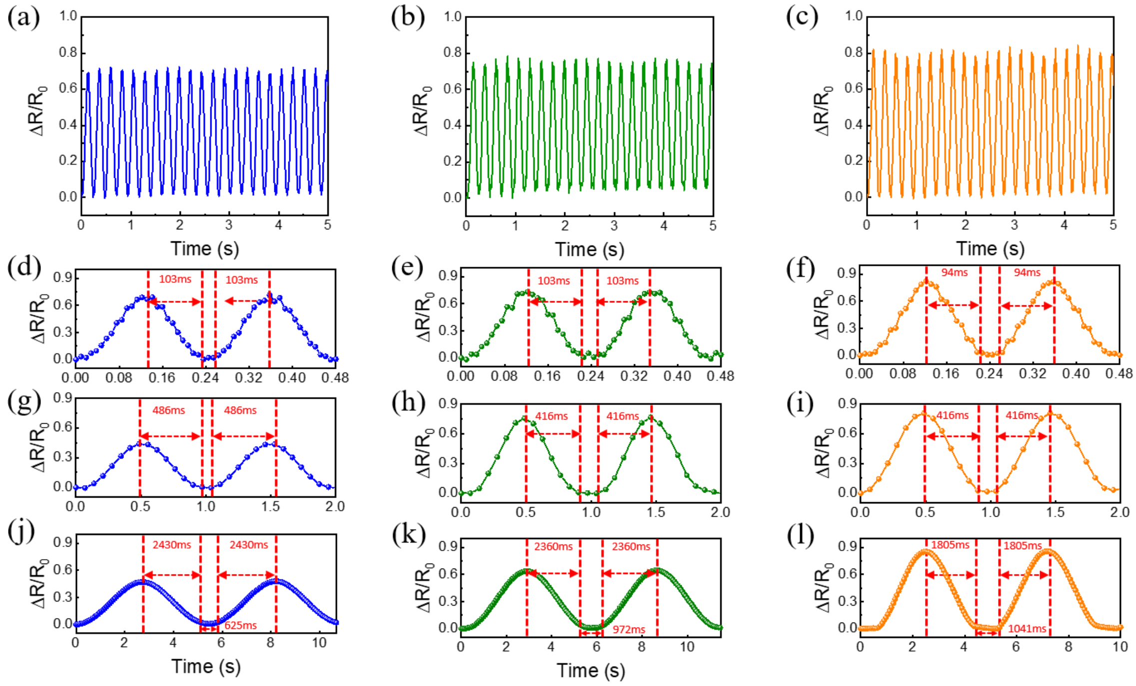

Figure S9. Response signals of the sensors during cyclic stretch–release motions at 50% strain under different strain rates: (a, d) IC, (b, e) MC 3, and (c, f) DMC 3 at 4.33Hz; (g) IC, (h) MC 3, and (i) DMC 3 at 1 Hz; (j) IC, (k) MC 3, and (l) DMC 3 at 0.17 Hz.

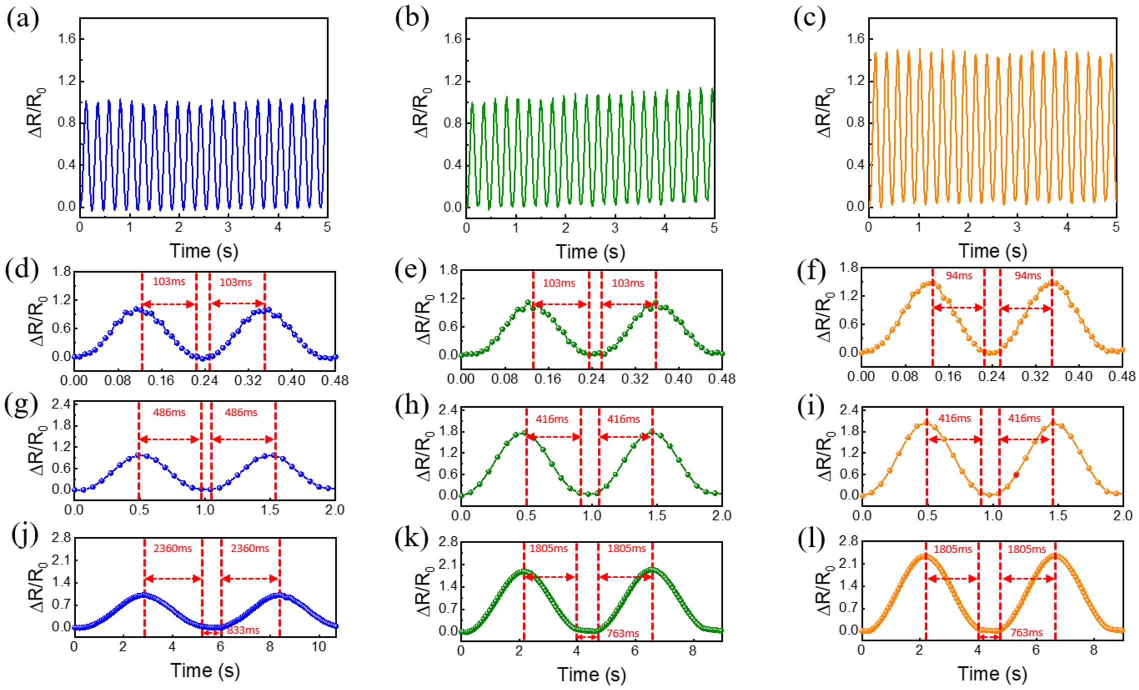

Figure S10. Response signals of the sensors during cyclic stretch–release motions at 100% strain under different strain rates: (a, d) IC, (b, e) MC 3, and (c, f) DMC 3 at 4.33Hz; (g) IC, (h) MC 3, and (i) DMC 3 at 1 Hz; (j) IC, (k) MC 3, and (l) DMC 3 at 0.17 Hz.

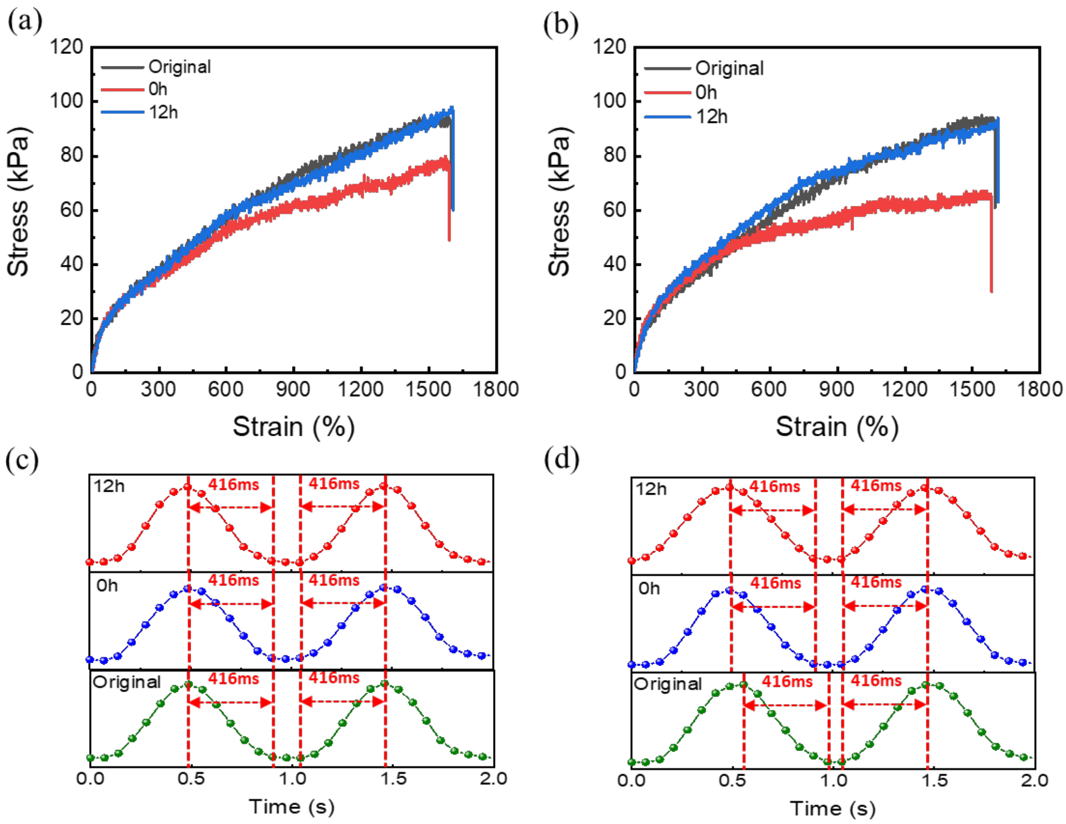

Figure S11. Stress–strain curves and response signals of the uncut MC 3 sensor after autonomous recovery following 100,000 cycles at 1 Hz under strains of (a, c) 50% and (b, d) 100% strain.

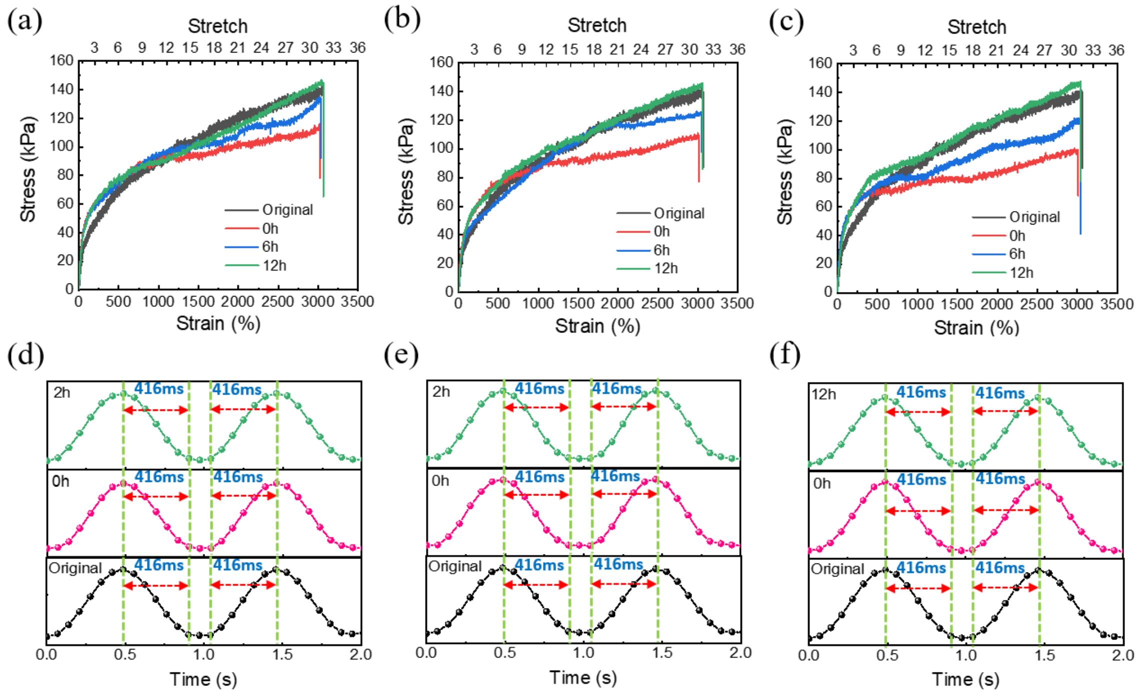

Figure S12. Stress–strain curves and response signals of the uncut DMC 3 sensor after autonomous recovery following 100,000 stretch–release cycles at 1 Hz under strains of (a, c) 50%, (b, d) 100%, and (c, f) 150%.

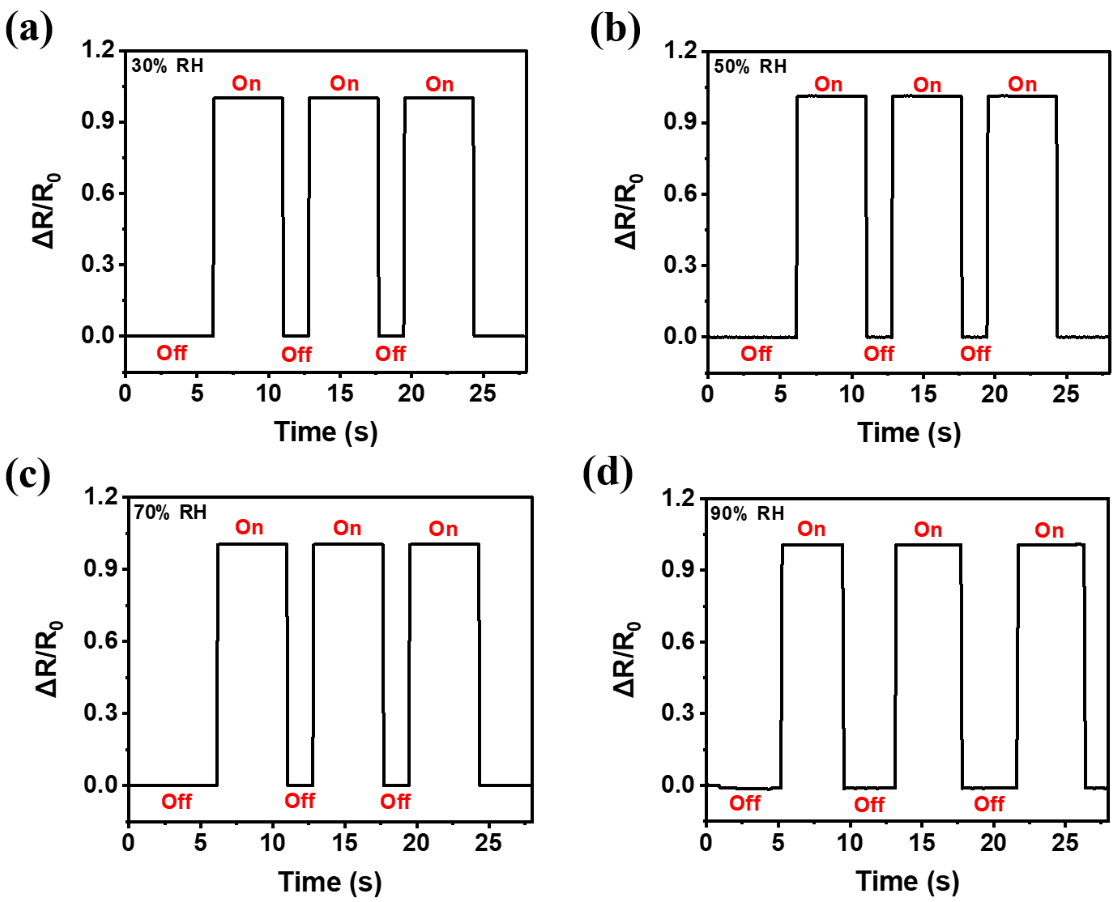

Figure S13. Relative resistance changes ($\Delta R/R_0$) of DMC 3 sensors measured at room temperature under varying relative humidity conditions: (a) 30% RH, (b) 50% RH, (c) 70% RH, and (d) 90% RH. The sensors were placed in a temperature-controlled chamber and stabilized at each humidity level for 5 minutes before applying repeated on-off cycles to obtain $\Delta R/R_0$ from the I-V curve. The measurements indicate minimal resistance variation across the tested humidity range, highlighting the humidity-resistant performance of DMC 3 sensors.

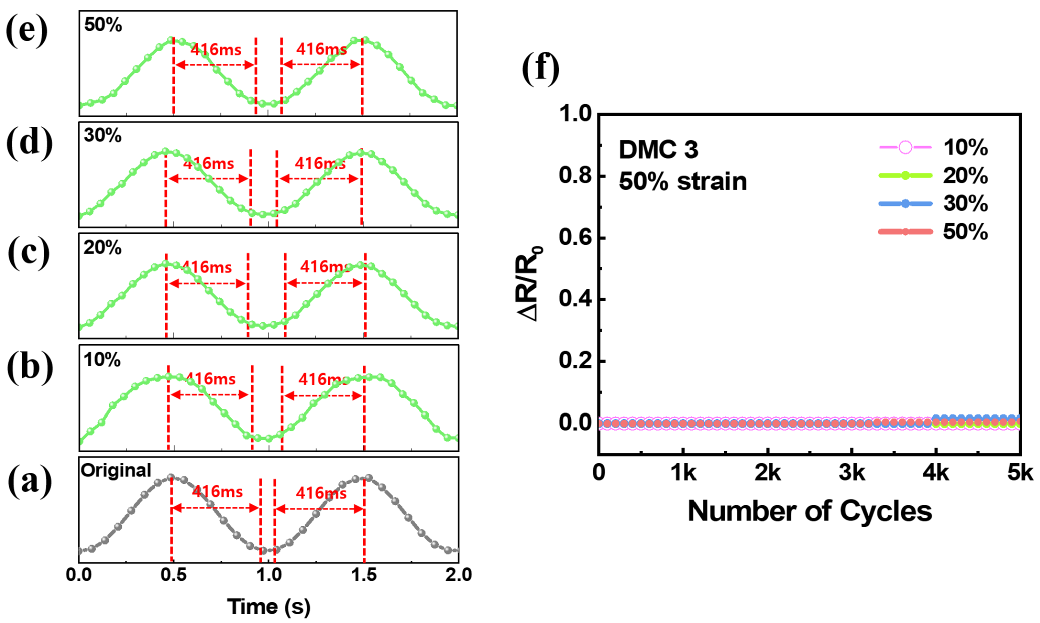

Figure S14. Relative resistance changes ($\Delta R/R_0$) of DMC 3 sensors at room temperature under different swelling ratios: (a) original, (b) 10%, (c) 20%, (d) 30%, (e) 50%, and (f) $\Delta R/R_0$ versus stretching cycles at different swelling ratios.

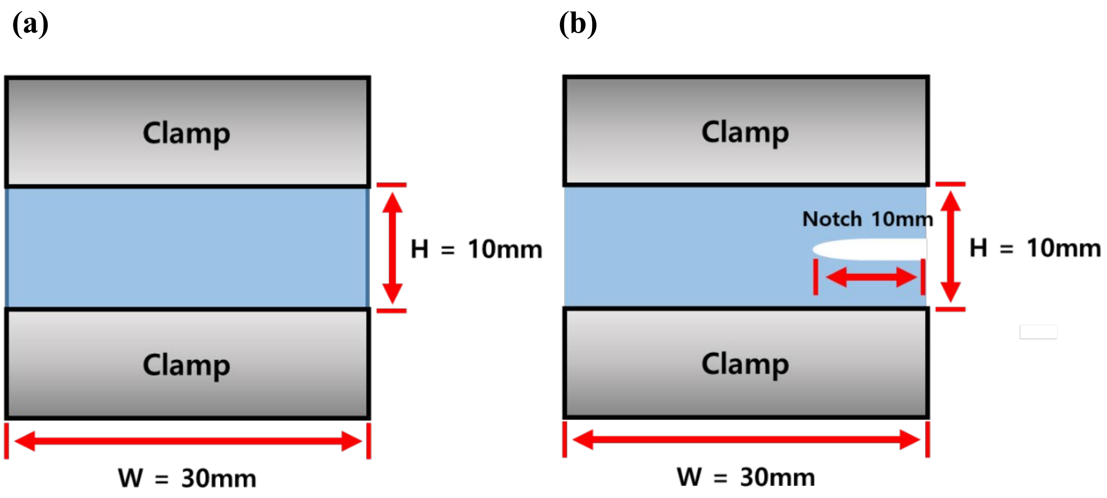

Figure S15. Schematic of fatigue cyclic test conditions for (a) uncut and (b) pre-cut sample with single notch. Rectangular samples (50×30×1.0 mm^3) were clamped in two rigid grips and mounted in a tensile testing machine with a 100 N load cell. The length (H = 10 mm) and width (W = 30 mm) of samples in the undeformed state were used for cyclic stretch tests. Fatigue-resistance tests were performed using the single-notch method with a 10 mm pre-cut crack length, subjected to cyclic stretching at maximum stretch (λ_{max}) at a crosshead speed of 750 mm/min.

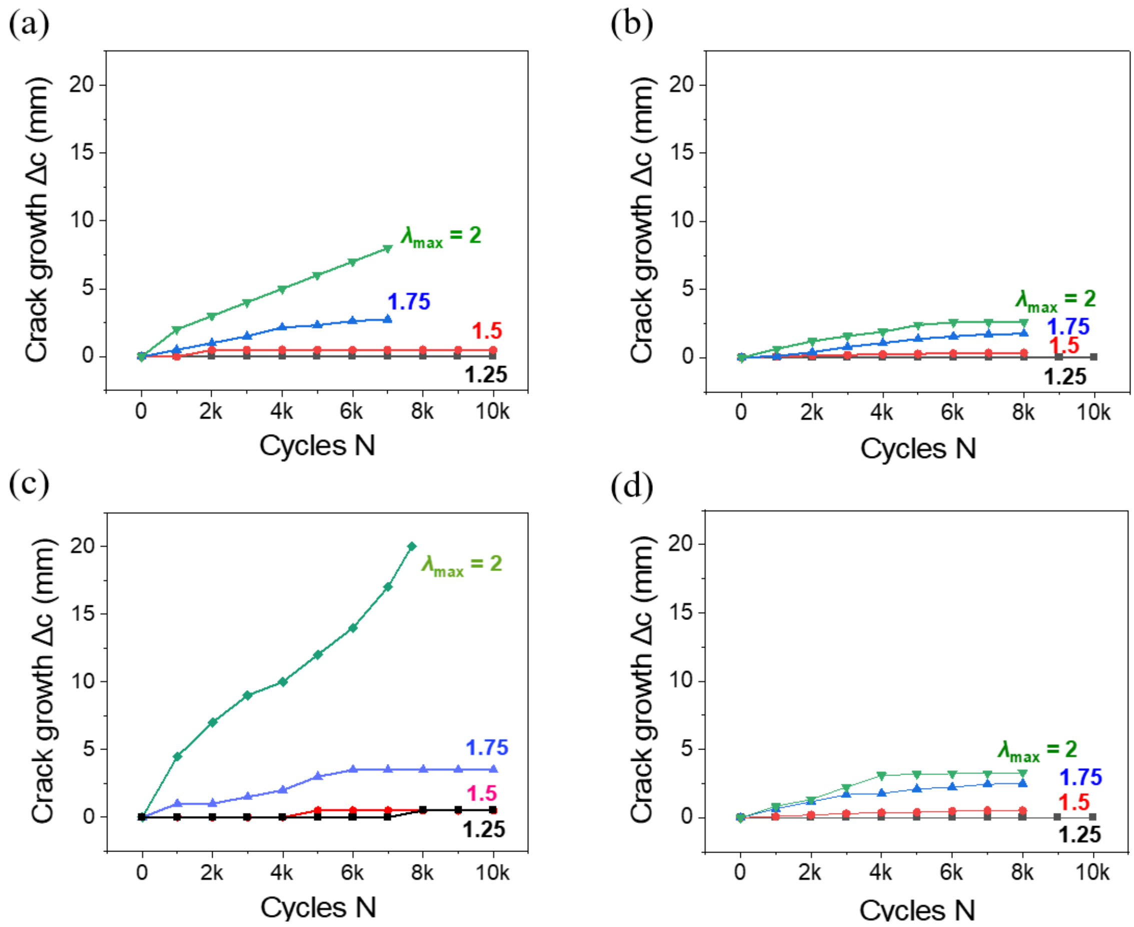

Figure S16. Crack growth (Δc) with fatigue cycles (N) at various λ_{max} levels for single-notch sensors: (a) IC, (b) DIC, (c) MC 3, and (d) DMC 3.

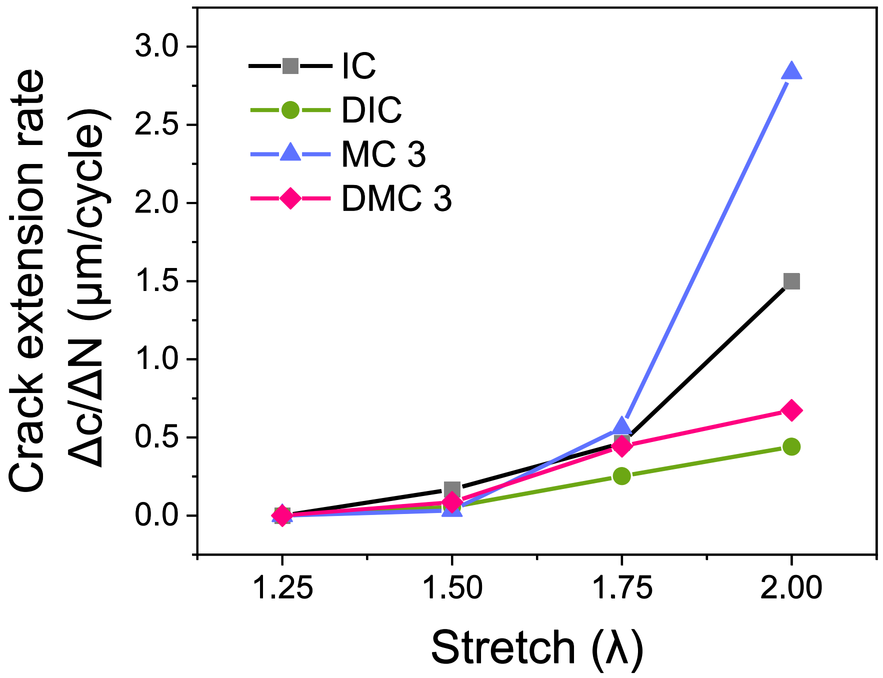

Figure S17. Variation of crack extension rate (Δc/ΔN) with stretch (λ_{max}) for single-notch sensors.

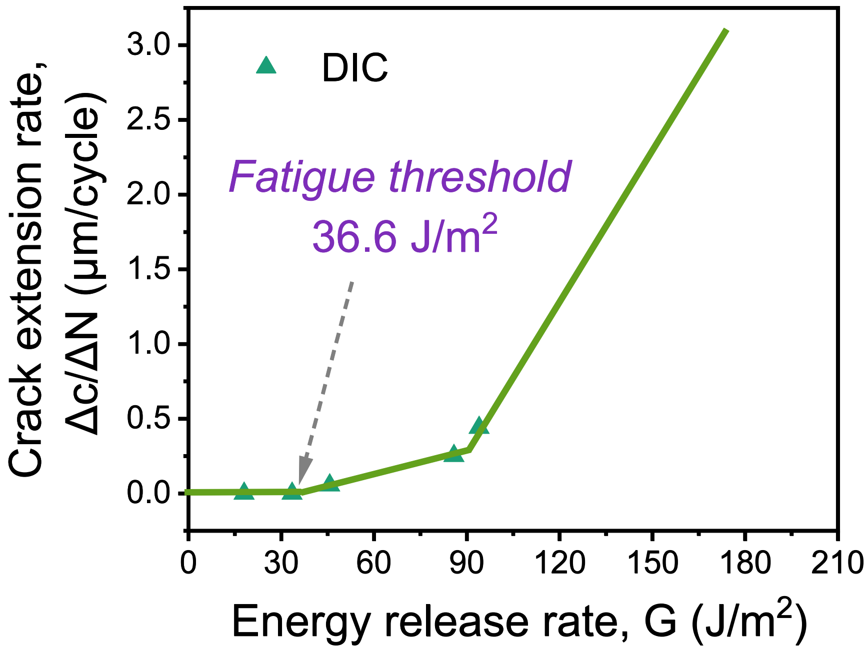

Figure S18. Crack extension rate (Δc/ΔN) as a function of energy release rate (*G*) and fatigue threshold (G_c) for the single-notch DIC sensor.

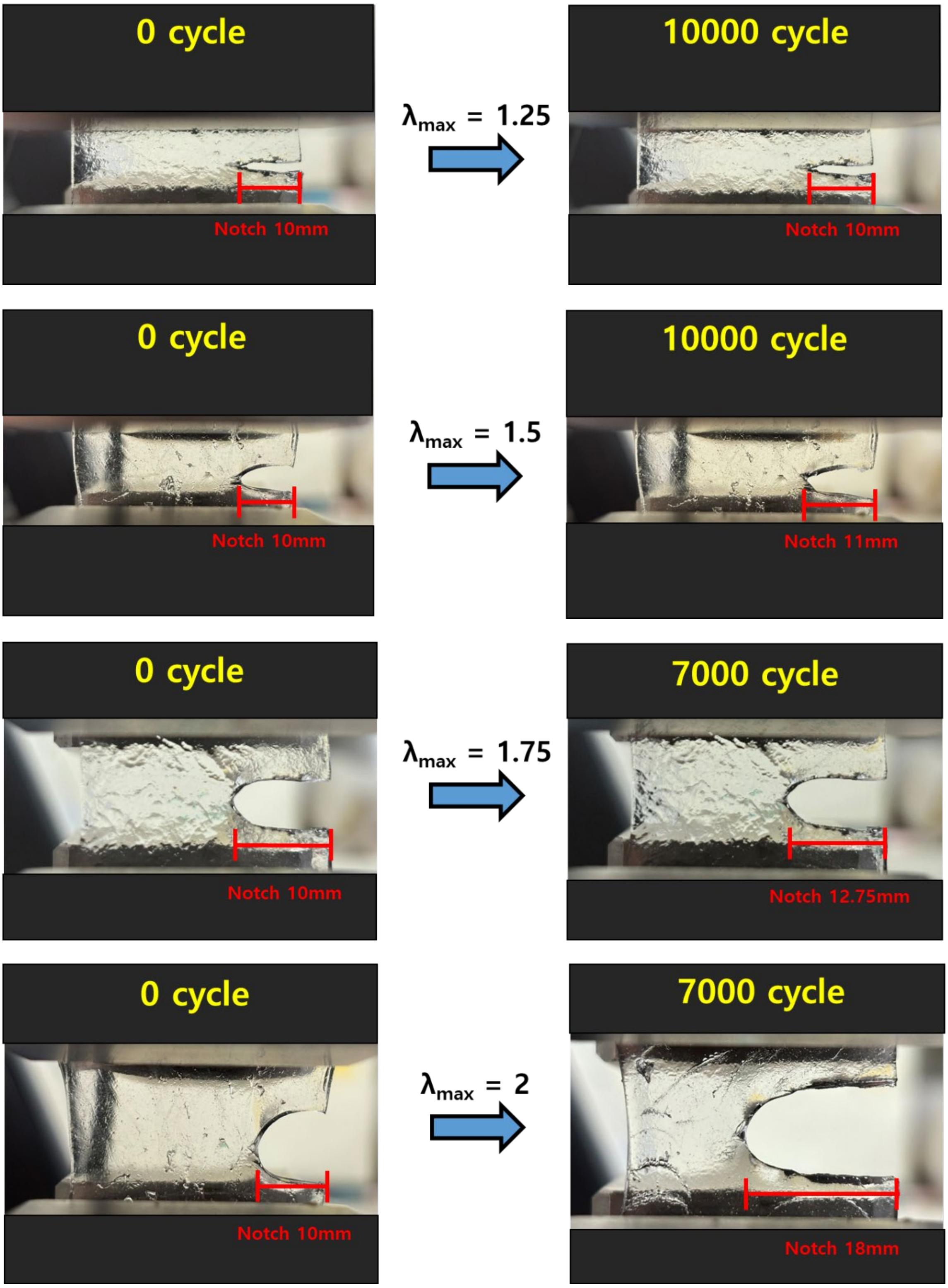

Figure S19. Progression of pre-crack length in single-notch IC sensors during fatigue cycling tests at various λ_{max} levels.

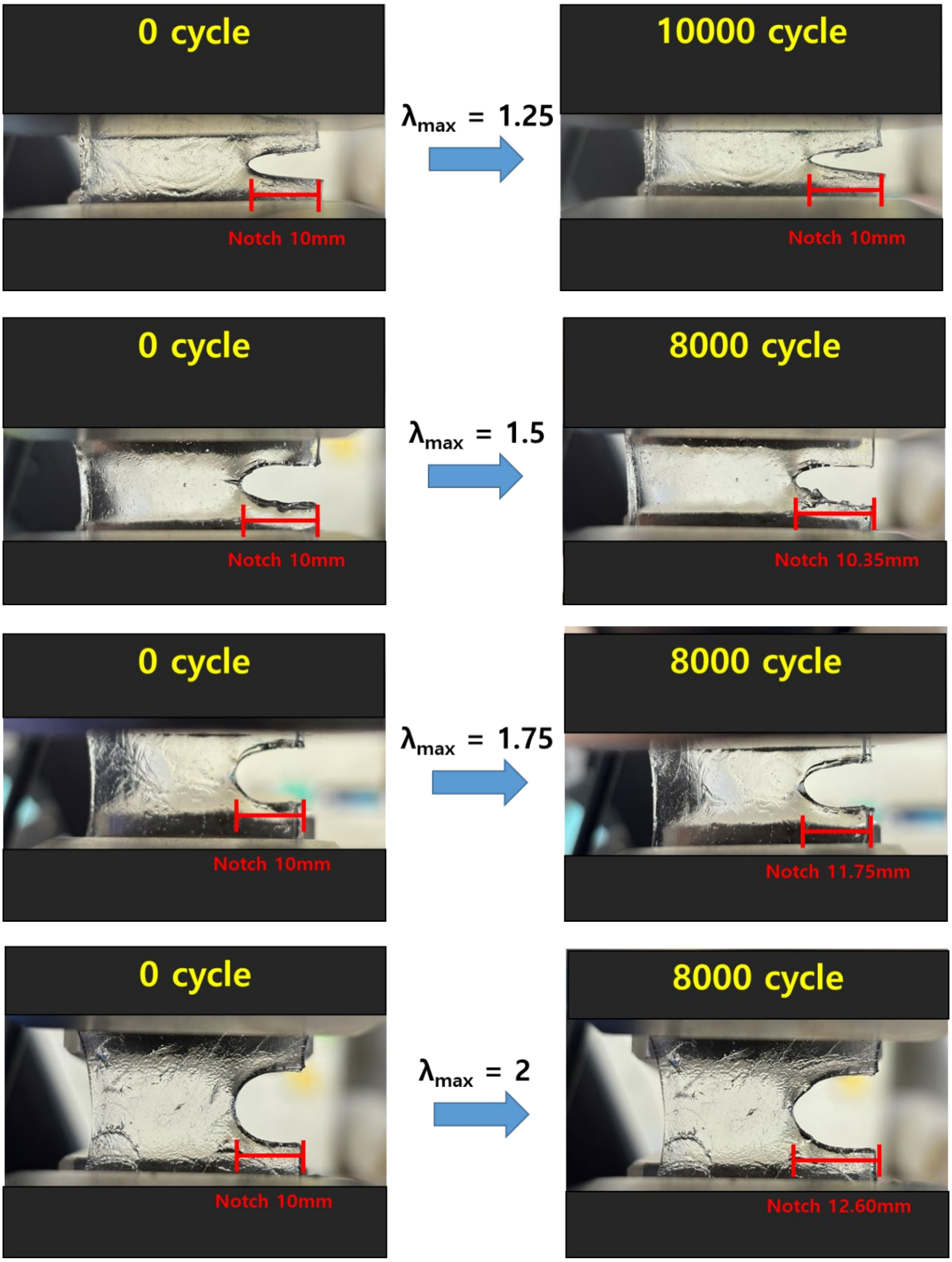

Figure S20. Progression of pre-crack length in single-notch DIC sensors during fatigue cycling tests at various λ_{max} levels.

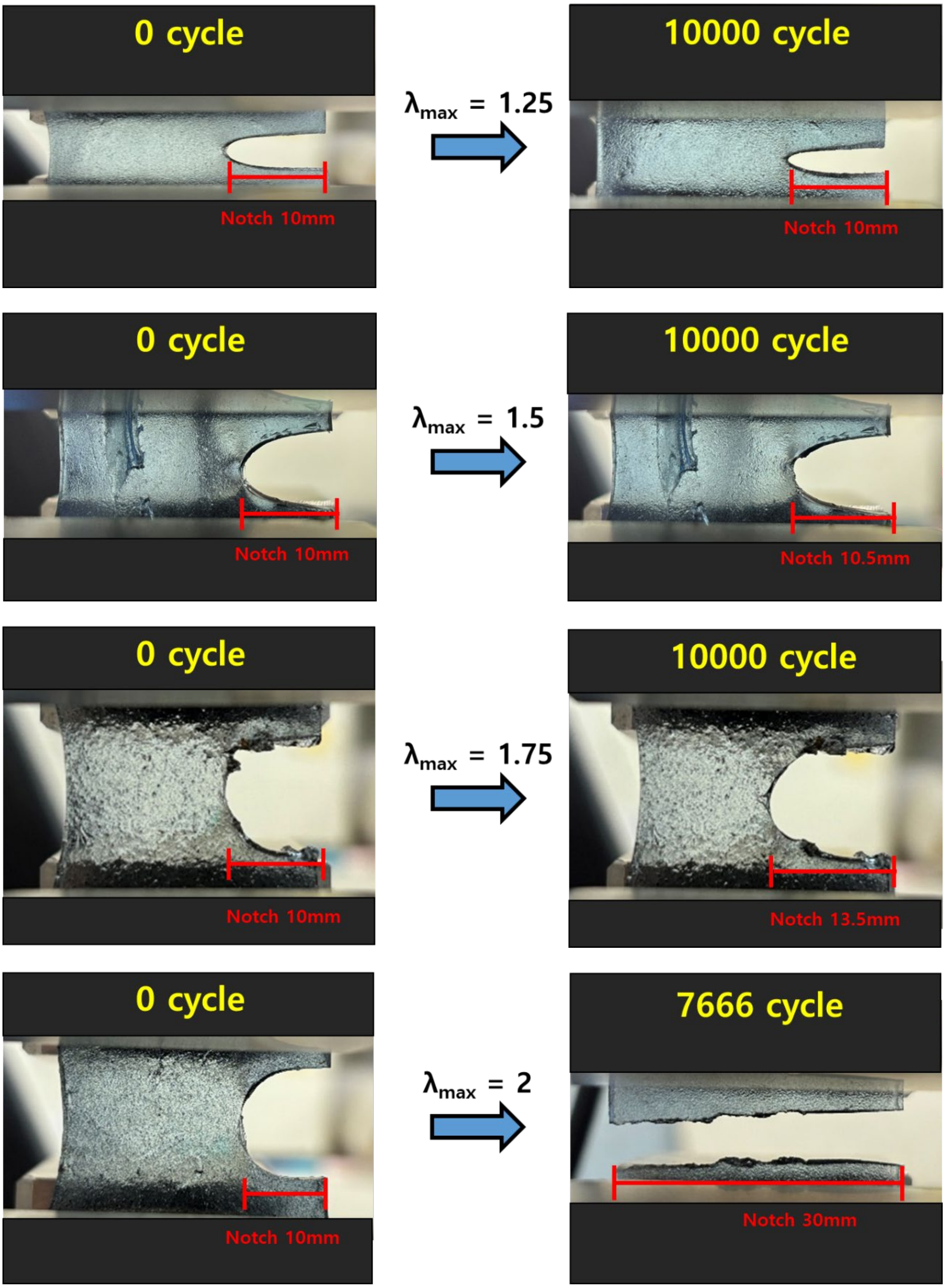

Figure S21. Progression of pre-crack length in single-notch MC 3 sensors during fatigue cycling tests at various λ_{max} levels.

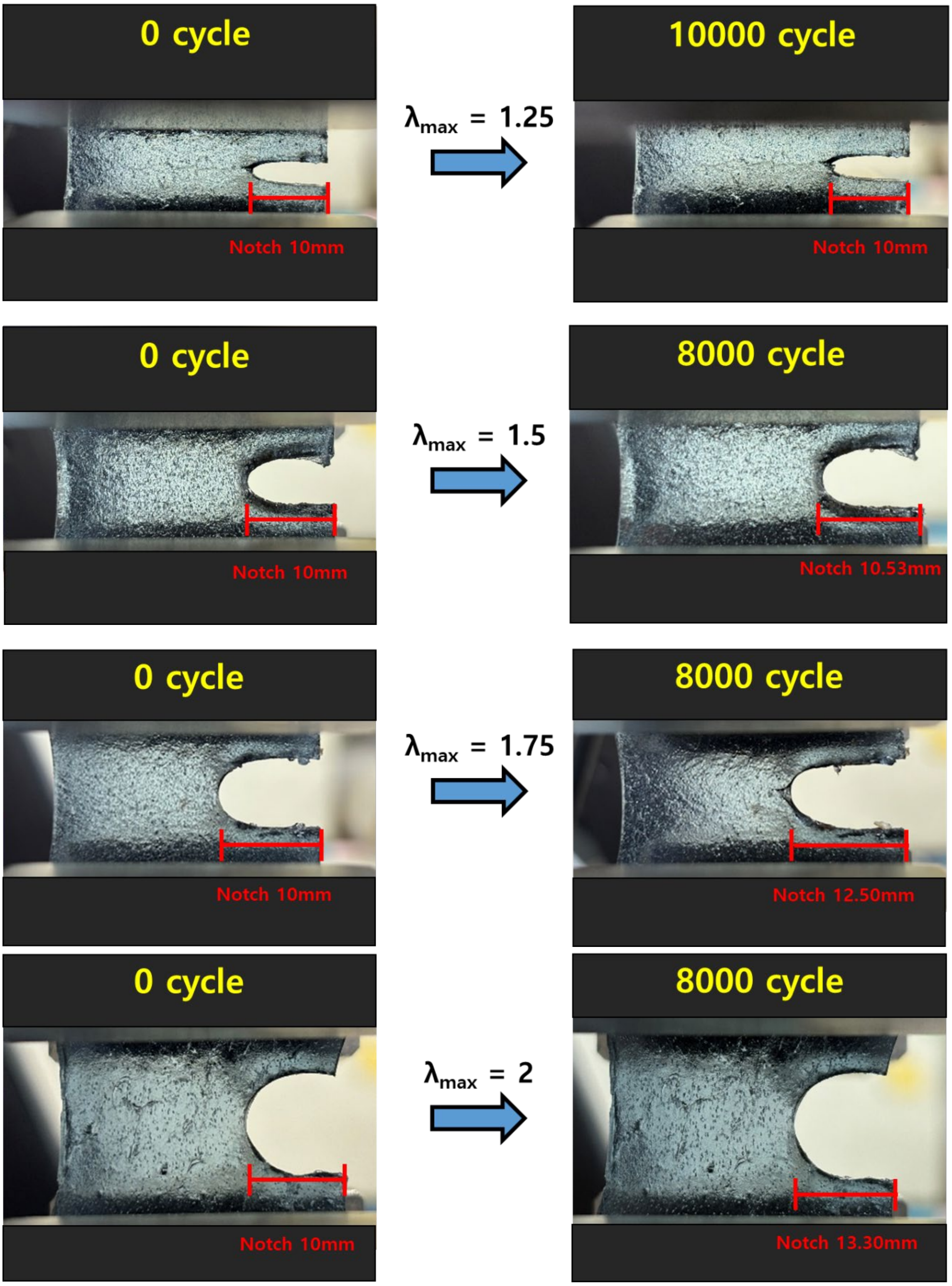

Figure S22. Progression of pre-crack length in single-notch DMC 3 sensors during fatigue cycling tests at various λ_{max} levels.

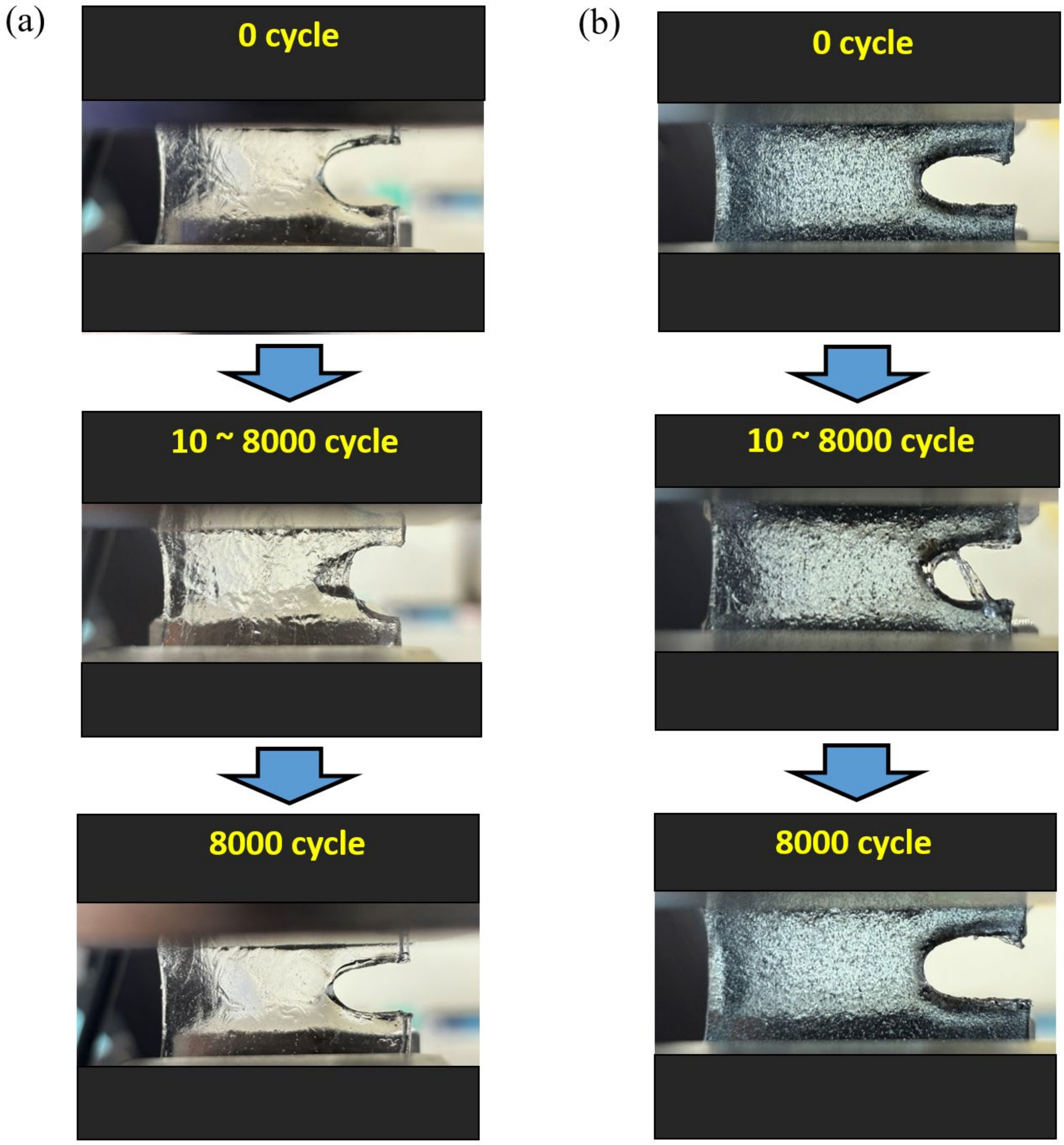

Figure S23. Photographs showing self-healing of (a) single-notch DIC at λ_{max}=1.75 and (b) single-notch DMC 3 at λ_{max}=1.5 during cyclic stretching from 10 to 8,000 cycles.

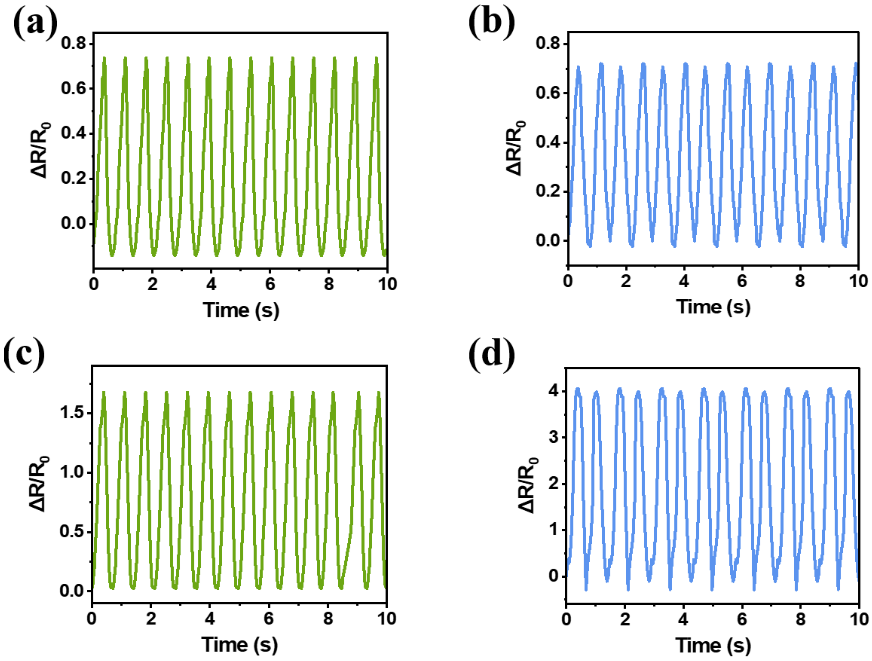

Figure S24. Response signals from the skin-attached DMC 3 sensors with different swelling ratios monitoring various human physiological movements. Ankle movements: (a) 10% and (c) 50%; Wrist movements: (b) 10% and (d) 50%.

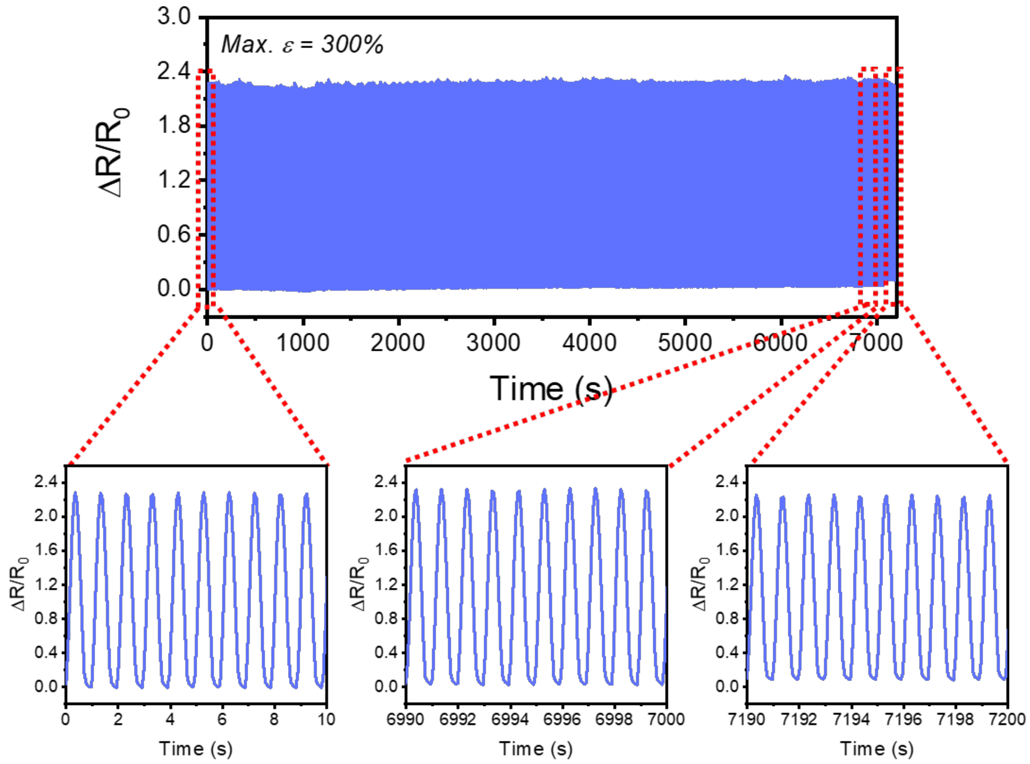

Figure S25. Relative resistance changes of the uncut DMC 3 sensor over 7,000 stretch-release cycles under 300% strain ($\lambda_{max} = 4$) at 1 Hz (top). The bottom graph shows the stable resistance response of the DMC 3 sensor during cyclic testing.

Supplementary References

[1] J.H. Lim, M.J. Kim, H.G. Yoon, S.W. Kim, *Compos. B Eng.* **2022**, 247, 110299.

[2] Shen Z, Zhang Z, Zhang N, Li J, Zhou P, Hu F, et al. High-Stretchability, Ultralow-Hysteresis ConductingPolymer Hydrogel Strain Sensors for Soft Machines. Advanced Materials 2022;34. https://doi.org/10.1002/adma.202203650.

[3] Lam TN, Lee GS, Kim B, Dinh Xuan H, Kim D, Yoo S Il, et al. Microfluidic preparation of highly stretchable natural rubber microfiber containing CNT/PEDOT:PSS hybrid for fabric-sewable wearable strain sensor. Compos Sci Technol 2021;210. https://doi.org/10.1016/j.compscitech.2021.108811.

[4] Lee YY, Kang HY, Gwon SH, Choi GM, Lim SM, Sun JY, et al. A Strain-Insensitive Stretchable Electronic Conductor: PEDOT:PSS/Acrylamide Organogels. Advanced Materials 2016;28:1636–43. https://doi.org/10.1002/adma.201504606.

[5] Ryu J, Kim J, Oh J, Lim S, Sim JY, Jeon JS, et al. Intrinsically stretchable multi-functional fiber with energy harvesting and strain sensing capability. Nano Energy 2019;55:348–53. https://doi.org/10.1016/j.nanoen.2018.10.071.

[6] Bhattacharjee M, Soni M, Escobedo P, Dahiya R. PEDOT:PSS Microchannel-Based Highly Sensitive Stretchable Strain Sensor. Adv Electron Mater 2020;6. https://doi.org/10.1002/aelm.202000445.

[7] Ko S, Chhetry A, Kim D, Yoon H, Park JY. Hysteresis-Free Double-Network Hydrogel-Based Strain Sensor for Wearable Smart Bioelectronics. ACS Appl Mater Interfaces 2022;14:31363–72. https://doi.org/10.1021/acsami.2c09895.

[8] Liu S, Li L. Ultrastretchable and Self-Healing Double-Network Hydrogel for 3D Printing and Strain Sensor. ACS Appl Mater Interfaces 2017;9:26429–37. https://doi.org/10.1021/acsami.7b07445.

[9] S. Azadi, S. Peng, S. A. Moshizi, M. Asadnia, J. Xu, I. Park, C. H. Wang, S. Wu, Biocompatible and Highly Stretchable PVA/AgNWs Hydrogel Strain Sensors for Human Motion Detection. Adv Mater Technol 2020;5. https://doi.org/10.1002/admt.202000426.

[10] Giffney T, Bejanin E, Kurian AS, Travas-Sejdic J, Aw K. Highly stretchable printed strain sensors using multi-walled carbon nanotube/silicone rubber composites. Sens Actuators A Phys 2017;259:44–9. https://doi.org/10.1016/j.sna.2017.03.005.

[11] Chu X, Wang R, Zhao H, Kuang M, Yan J, Wang B, et al. Cross-Links-Entanglements Integrated Networks Contributing to Highly Resilient, Soft, and Self-Adhesive Elastomers with Low Hysteresis for Green Wearable Electronics. ACS Appl Mater Interfaces 2022;14:16631–40. https://doi.org/10.1021/acsami.2c00828.

[12] Choi DY, Kim MH, Oh YS, Jung SH, Jung JH, Sung HJ, et al. Highly stretchable, hysteresis-free ionic liquid-based strain sensor for precise human motion monitoring. ACS Appl Mater Interfaces 2017;9:1770–80. https://doi.org/10.1021/acsami.6b12415.

[13] Zhang W, Zhang X, Zhao W, Wang X. High-Sensitivity Composite Dual-Network Hydrogel Strain Sensor and Its Application in Intelligent Recognition and Motion Monitoring. ACS Appl Polym Mater 2023;5:2628–38. https://doi.org/10.1021/acsapm.2c02215.

[14] Xu L, Liu S, Zhu L, Liu Y, Li N, Shi X, et al. Hydroxypropyl methyl cellulose reinforced conducting polymer hydrogels with ultra-stretchability and low hysteresis as highly sensitive strain sensors for wearable health monitoring. Int J Biol Macromol 2023;236. https://doi.org/10.1016/j.ijbiomac.2023.123956.

[15] Bian Z, Li Y, Sun H, Shi M, Zheng Y, Liu H, et al. Transparent, intrinsically stretchable cellulose nanofiber-

mediated conductive hydrogel for strain and humidity sensing. Carbohydr Polym 2023;301. https://doi.org/10.1016/j.carbpol.2022.120300.

[16] Feng E, Zheng G, Li X, Zhang M, Li X, Han X, et al. A toughened, transparent, anti-freezing and solvent-resistant hydrogel towards environmentally tolerant strain sensor and soft connection. Colloids Surf A Physicochem Eng Asp 2023;656. https://doi.org/10.1016/j.colsurfa.2022.130390.

[17] Asad Ullah Khalid M, Hwan Chang S. Characterization of highly linear stretchable sensor made of Gr-PEDOT:PSS/MnO2 nanowires/Ecoflex composite. Compos Struct 2023;311. https://doi.org/10.1016/j.compstruct.2023.116824.

[18] Liu K, Yang C, Song L, Wang Y, Wei Q, Alamusi, et al. Highly stretchable, superhydrophobic and wearable strain sensors based on the laser-irradiated PDMS/CNT composite. Compos Sci Technol 2022;218. https://doi.org/10.1016/j.compscitech.2021.109148.

[19] Zhan P, Jia Y, Zhai W, Zheng G, Dai K, Liu C, et al. A fibrous flexible strain sensor with Ag nanoparticles and carbon nanotubes for synergetic high sensitivity and large response range. Compos Part A Appl Sci Manuf 2023;167. https://doi.org/10.1016/j.compositesa.2023.107431.

[20] Yazdani S, Khan M, Shahzad A, Shah LA, Ye D. Ionic conductive hydrogels formed through hydrophobic association for flexible strain sensing. Sens Actuators A Phys 2023;350. https://doi.org/10.1016/j.sna.2022.114148.

[21] Wen N, Guan X, Fan Z, Guo Y, Cong T, Huang H, et al. A highly stretchable and breathable self-powered dual-parameter sensor for decoupled temperature and strain sensing. Org Electron 2023;113. https://doi.org/10.1016/j.orgel.2022.106723.

[22] Park H, Kim DS, Hong SY, Kim C, Yun JY, Oh SY, et al. A skin-integrated transparent and stretchable strain sensor with interactive color-changing electrochromic displays. Nanoscale 2017;9:7631–40. https://doi.org/10.1039/c7nr02147j.

[23] Wang Y, Jia Y, Zhou Y, Wang Y, Zheng G, Dai K, et al. Ultra-stretchable, sensitive and durable strain sensors based on polydopamine encapsulated carbon nanotubes/elastic bands. J Mater Chem C Mater 2018;6:8160–70. https://doi.org/10.1039/c8tc02702a.

[24] Yang Y, Shi L, Cao Z, Wang R, Sun J. Strain Sensors with a High Sensitivity and a Wide Sensing Range Based on a Ti 3 C 2 T x (MXene) Nanoparticle–Nanosheet Hybrid Network. Adv Funct Mater 2019;29. https://doi.org/10.1002/adfm.201807882.

[25] Fan X, Wang N, Wang J, Xu B, Yan F. Highly sensitive, durable and stretchable plastic strain sensors using sandwich structures of PEDOT:PSS and an elastomer. Mater Chem Front 2018;2:355–61. https://doi.org/10.1039/c7qm00497d.

[26] Yang Y, Cao Z, He P, Shi L, Ding G, Wang R, et al. Ti3C2Tx MXene-graphene composite films for wearable strain sensors featured with high sensitivity and large range of linear response. Nano Energy 2019;66. https://doi.org/10.1016/j.nanoen.2019.104134.

[27] Shi G, Liu T, Kopecki Z, Cowin A, Lee I, Pai J-H, et al. A Multifunctional Wearable Device with a Graphene/Silver Nanowire Nanocomposite for Highly Sensitive Strain Sensing and Drug Delivery. C (Basel) 2019;5:17. https://doi.org/10.3390/c5020017.

[28] Wang Y, Hao J, Huang Z, Zheng G, Dai K, Liu C, et al. Flexible electrically resistive-type strain sensors based on reduced graphene oxide-decorated electrospun polymer fibrous mats for human motion monitoring. Carbon N Y 2018;126:360–71. https://doi.org/10.1016/j.carbon.2017.10.034.

[29] Liu P, Pan W, Liu Y, Liu J, Xu W, Guo X, et al. Fully flexible strain sensor from core-spun elastic threads with integrated electrode and sensing cell based on conductive nanocomposite. Compos Sci Technol

2018;159:42–9. https://doi.org/10.1016/j.compscitech.2018.02.034.

[30] Liu X, Tang C, Du X, Xiong S, Xi S, Liu Y, et al. A highly sensitive graphene woven fabric strain sensor for wearable wireless musical instruments. Mater Horiz 2017;4:477–86. https://doi.org/10.1039/c7mh00104e.